LUND UNIVERSITY

FACULTY OF SCIENCE

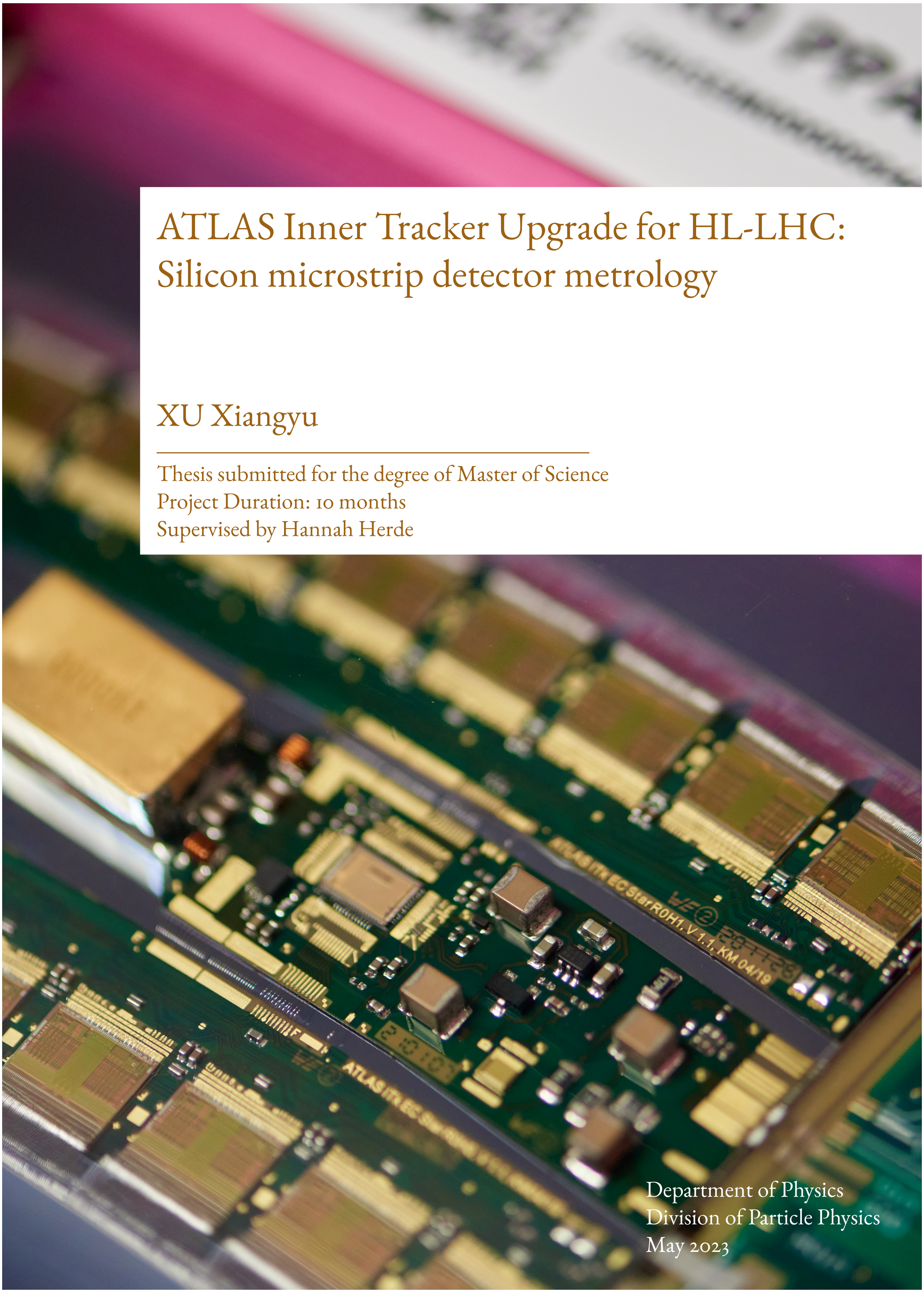

ATLAS Inner Tracker Upgrade for HL-LHC: Silicon microstrip detector metrology

XU Xiangyu

Thesis submitted for the degree of Master of Science
Project Duration: 10 months
Supervised by Hannah Herde

Department of Physics
Division of Particle Physics
May 2023

ABSTRACT

The Large Hadron Collider (LHC) will be upgraded to the High-Luminosity LHC (HL-LHC) by the end of this decade, with five times larger luminosity and 200 inelastic collisions per proton-proton bunch crossing. Thus, the ATLAS detector is challenged to survive the stronger radiation and the increased particle flux. As a result, the new ATLAS Inner Tracker (ITk) will replace the current one with a new full-silicon detector. The new detector requires high precision during manufacturing. Thus, a metrology process is necessary, in which an optical zoom microscope with precise position measurement is used. A post-process program has been created to handle the measuring results. Validation and tests for this method for several types of the sensor have been done in this project in Lund, Uppsala and Copenhagen.

POPULAR ABSTRACT

The primary goal of this project is to demonstrate the measurement of the position of the electronics on a silicon sensor with a commercial tool with a zoom-microscope and precise moving table, known as the SmartScope. This kind of sensor will replace the current inner-most detector in CERN's largest collider, namely the Large Hadron Collider (LHC), as the upgrade will finish by the end of this decade. This upgrade will multiply the flux of protons in each collision, and will require the new detector to have a stronger tolerance to the radiation and the large amount of particles per collision. A new silicon sensor with sub-millimetre segments is developed, and the fine bonding between the electronics and the silicon sensor requires the quality control process in this project.

KEYWORDS: High energy physics experiment; LHC; HL-LHC; ATLAS; ITk; Metrology; Measurement

Contents

Chapter 1

Introduction

1.1 Standard Model

With the mathematical contribution led by Yang and Mills[1] and the experimental achievements of Wu, Glashow[2], Weinberg[3] and Salam[4] developed a theory that combined electromagnetic and weak interactions and introduced the Higgs mechanism to the electroweak interaction, namely the Standard Model. The Standard Model predicted a few particles at that time, and they were discovered one by one, like the top quark in 1995 in Fermilab[5][6] or the tau neutrino in 2000[7], leaving the Higgs boson the last missing puzzle.

The search for the Higgs boson led to the construction of the LHC (Large Hadron Collider), as the major scientific goals of the LHC are to study the Higgs mechanism, to search for any candidates of the supersymmetry theory, to learn about the dark matter and so on.[8][9]

1.2 The LHC

The LHC is the largest particle collider in the world. The LHC is the most advanced facility for the investigation of the structure of matter at the smallest scale.[10]

The LHC aims to answer several fundamental questions, i.e. the origin of mass, the nature of the dark matter, new forces and particles, etc. In 2012, the LHC collaboration announced the discovery of a new particle, which was confirmed to be the Higgs boson[11][12]. The discovery and studies of the Higgs boson greatly enlarged our understanding of the universe and provided new and unique insights into the fundamental structure of matter and the origin of mass[10]. Since the first data acquisition in 2010, the accelerator has delivered collisions at an increasing rate. The collider also reached the highest energy ever in colliders, proton-proton collisions at 13.6 TeV in the centre-of-mass frame in 2022.

With proposals like the Future Circular Collider, the Circular Electron Positron Collider and the International Linear Collider still in draft, LHC will still be at the forefront of high energy physics for the next 20 years.[10] Thus, the full exploitation of the LHC, as well as the upgraded High Luminosity LHC (HL-LHC) has been given the highest priority by the international high energy physics community.[10][13]

The HL-LHC upgrade will start in 2026, after the LHC reached 14 TeV collision energy after two long shutdowns, namely LS1 and LS2. In 2015, LS1 was completed to prepare the accelerator for operation at its design energy and luminosity, and in 2021, LS2 was completed with significant detector upgrades, known as Phase-I.[10]

Long Shutdown 3 (LS3) is supposed to start in 2026, which will include major performance upgrades of the accelerator for the HL-LHC, which requires the replacement of several major detector components.[10]

The luminosity describes the density of collisions, as the definition of it is the amount of particles in a cross-beam that travels through a certain area within a certain period of time. With a nominal luminosity of $\mathcal{L} = 5 \times 10^{34}\ \mathrm{cm}^{-2}\mathrm{s}^{-1}$ and an ultimate luminosity of $\mathcal{L} = 7.5 \times 10^{34}\ \mathrm{cm}^{-2}\mathrm{s}^{-1}$, HL-LHC will present an extremely challenging environment to the ATLAS experiment, well beyond that for which it was designed[14][10]. The current ATLAS inner tracking detector would be inoperable under such increased luminosity, and the detector itself has reached the end of its service life. Thus, the ATLAS collaboration decided to replace the inner detector with a new full-silicon tracking detector, namely Inner Tracker (ITk), which can survive the harsh radiation environment and improve the segmentation.[10]

1.3 Frame & Detector

No matter in the current tracking detector or in the ITk to be installed, segmented silicon pixel sensors and microstrip sensors are used as the detecting element. The silicon microstrip detector of the ITk, with a typical size of $10\ \mathrm{cm} \times 10\ \mathrm{cm}$, is fabricated in a way that the silicon has many segments that represent detector channels. In the case of the HL-LHC ATLAS ITk microstrip, such segmentation would provide a few thousand of channels each, and each channel represents an area with a width of tens of micrometres and a length of a few centimetres. All of the channels are to be wire-bonded to the front-end application-specific integrated circuits (ASICs), and in this case, ATLAS Binary Chips (ABCStar). That is to say, there will be a few thousand bonds to be wire-bonded on each sensor, and the sensors will be mass-produced. The total number of microstrip detectors would also be over 17 thousands.[10]

Certain manufacturing techniques were already developed and applied to prototype modules. However, the mounting for the electronics to the sensor is still highly position-sensitive as the bonds are densely populated. Thus, the electronic and metrology tests are necessary for the quality control of the electronics and combined modules before and after the mounting process, so that it can be confirmed that all of the sensors will work properly and uniformly after installation.

Chapter 2

Modules

As mentioned in Chap.1, the current ATLAS innermost tracking detector will be replaced with a new design to accommodate the higher luminosity in the upgrade to the HL-LHC. The solution includes a series of silicon microstrip detectors as well as a more internal array of pixel detectors. This project focuses on the metrology of the microstrip modules. Therefore, it is essential to understand the structure of the new detector modules.

2.1 Modules

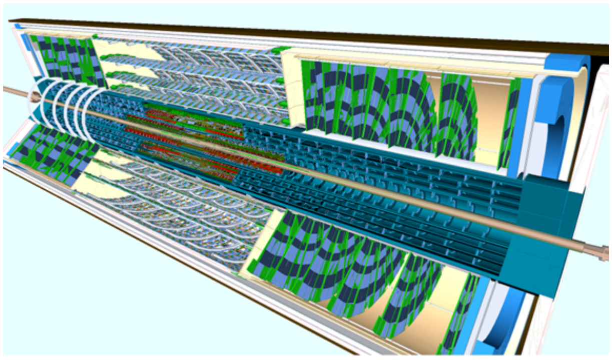

Figure 2.1: A visualisation of the ITk.[10]

As the name suggests, the Inner Tracker is the innermost sub-detector of the ATLAS experiment. ITk consists of four layers of silicon microstrip detectors and five layers of silicon pixel detectors. The initiated targets of this trajectory detector are reconstruction of charged particles, primary and secondary vertex identification and particle identification via energy loss. Also, this innermost sub-detector should withstand the radiation from the continuous particle interaction. The solution is a combination of outer strip detectors and inner pixel detectors, which can be seen from Fig.2.1.[10]

The strip detectors of the ITk consists of the barrel and end-caps. Fig.2.2 shows the layout of the ITk Strip Detector. The ITk Strip Detector consists of four barrel layers and six end-cap layers on each side. The four barrel layers totally consist of 392 identical staves, which are single structures with 28 modules on two sides. Each end-cap disk consists of 32 identical petals, which consist of six different geometries. Fig.2.3 shows an example of a complete stave and petal.[10]

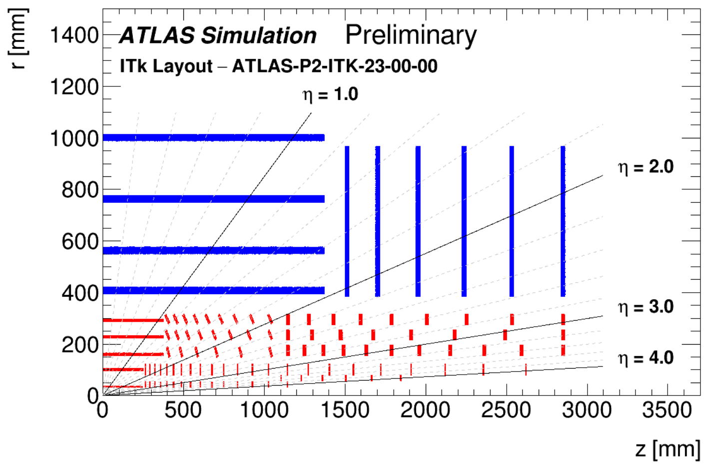

Figure 2.2: The Layout of the ITk Detector, with the pixel detectors in red and the strip detectors in blue.[15]

The fan shape of the petal requires different curvatures for the six different geometries, which are shown in Fig.2.4. Also, there are two different sensor patterns for the barrel stave detectors, as the inner two cylinders have 24.1 mm long short-strips, while the outer two have 48.2 mm long long-strips.[10]

As the smallest unit of the detector, each detector module hosts one silicon sensor and one or two low-mass printed circuit boards (PCBs) that hold the ASICs, namely ATLAS Binary Chip (ABCStar) and Hybrid Controller Chip (HCCStar). This PCB is known as the hybrid. Each complete module has a radiation-resistant power supply board on them, known as the powerboard (PB), which is shown as orange in the illustration of Fig.2.3.[10]

The ABCStars are connected with the silicon channels via wire bonds, as shown in Fig.2.5. Fig.2.6 shows the pre-production $R0$ module that arrived in Lund in March 2023, which clearly shows that each hybrid sits in the middle of a silicon sensor sector, which is divided into two smaller halves. By dividing the sensor into smaller regions, the channel length can be reduced and a better spatial resolution can be achieved.

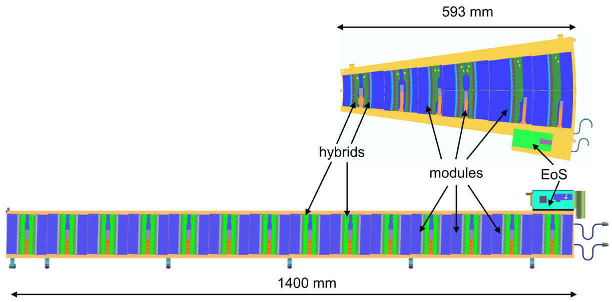

Figure 2.3: Local support components overview: End-cap petal (upper) and barrel stave (lower) components overview.[10]

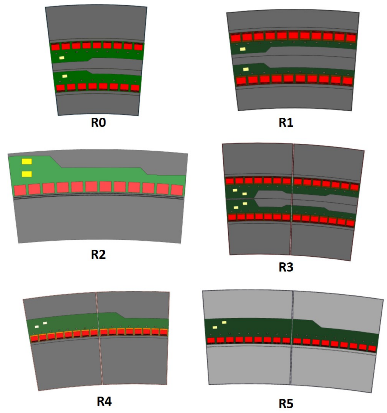

Figure 2.4: Overview of the different end-cap hybrids and sensor shapes.[10]

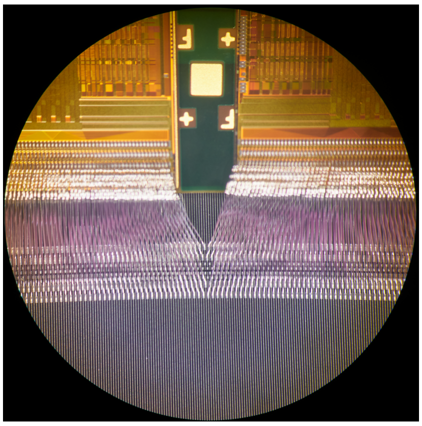

Figure 2.5: Module $R0$ prototype under microscope, here the wire bonds are clearly shown.

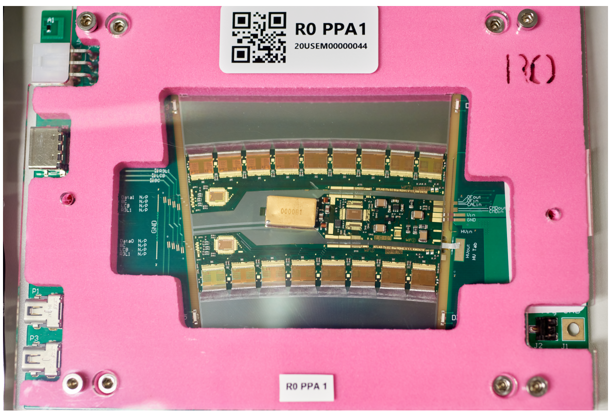

Figure 2.6: Module $R0$ prototype in a frame.

2.2 Metrology Tasks

As shown in Fig2.7, the module can be described as a segmented silicon board with several PCBs on it. Each ABCStar chip on the hybrid has 256 channels and each connects to a strip in the silicon. Meanwhile, a hybrid has seven to twelve ABCStar chips on it depending on the specific geometry. An $R0$ module, for example, has nine ABCStar chips on one hybrid. The average width of this module is at the magnitude of 100 mm, indicating the width of each channel segment is at the magnitude of 100 µm.

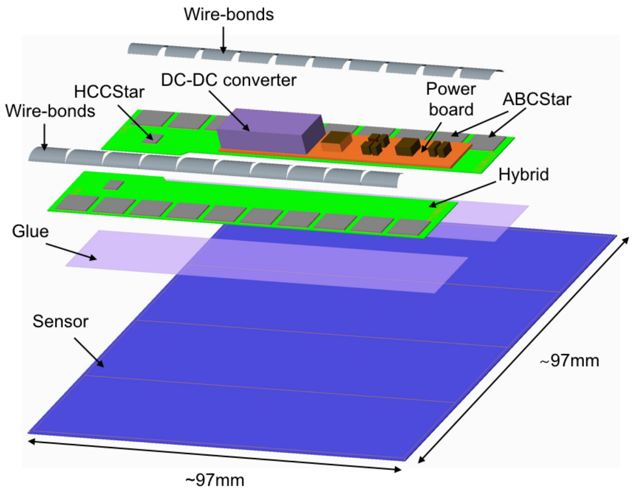

Figure 2.7: Exploded view of a short-strip barrel module with all relevant components.[10]

The goal of this project is to develop a routine to measure and define the three-dimensional position of each individual part on a module, and to determine if this module passes the metrology test. The tool used for measurement is an optical microscope with a precise moving table, known as the SmartScope produced by Optical Gaging Products. This machine will be discussed in detail in Sec.3.1.

The purpose for the metrology test is to make sure that the whole single module would perform as expected. As described in the technical document,[16]

1. The glue thickness under the hybrid and powerboard needs to be controlled for good electrical and thermos-mechanical performance.

2. The XY position of hybrids on the sensor needs to be controlled so that...

   ...the wirebonding is possible;

...the hybrids will not be glued over the guard-ring on the sensor;

...the module will not clash with neighbouring ones.

3. The XY position of powerboard on the sensor needs to be controlled so that...

   ...the powerboard will not be glued over the guard-ring on the sensor;

   ...the module will not clash with neighbouring ones.

4. The height of both hybrids and powerboard should be controlled so that the module will not clash with neighbouring ones.

5. The module bow should be controlled so that...

   ...the gluing process can be controlled;

   ...the thermal performance falls within expectation;

   ...the module will not clash with neighbouring ones.

It is worth noting that, in this project, the module bow is not involved. Thus this project only focuses on the XYZ position of the hybrids and the powerboard, in reference to the sensor plane.

Hence there are the limits for the positioning:

1. For XY position for hybrids and powerboards,

   $|\Delta X| < 0.25\,\mathrm{mm}$

   $|\Delta Y| < 0.25\,\mathrm{mm}$

2. For Z position for hybrids and powerboards,

   pass within 70 µm-170 µm;

   pass with problems within 40 µm-70 µm;

   fails otherwise.

2.2.1 Procedure

Module metrology occurs before wire bonding since its primary objective is to validate that the module's geometry allows bonding. The whole procedure of the metrology measurement is discussed in Chap.4, and here only the brief list is given.

The first thing is to set up the measurement coordinate system, which overwrites the coordinate system default in the SmartScope. All measurements will be conducted in reference to this coordinate system. The coordinate system is always based on the same feature on the

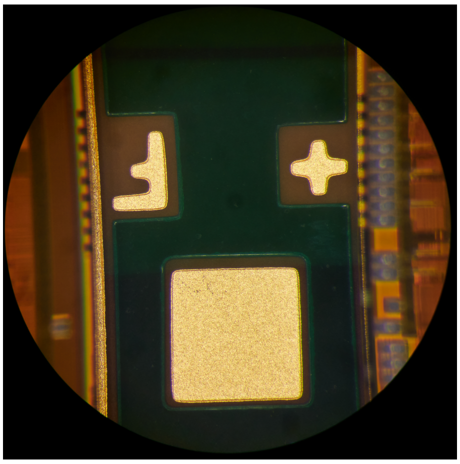

Figure 2.8: Two fiducial marks between two ABCStar ASICs under microscope.

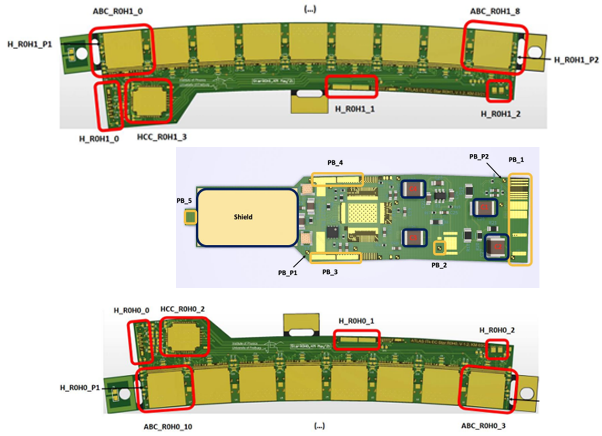

Figure 2.9: The parts to be measured on the $R0$ components.[16]

silicon sensor. The coordinate system is always defined by the corners of a sensor, as shown in Fig.4.1 and it will be discussed with details in Sec.4.1.

Then the position of the hybrids and powerboards will be measured. The position of all these PCBs is defined by two certain fiducial marks, which are the leftmost and rightmost ones. Fig.2.8 shows a pair of the fiducial marks on a hybrid between ABCStars.

For the height measurement, many more measurement points are used. First of all, the reference plane on the silicon sensor is to be taken. In principle, at least four points that create a square with the hybrid and powerboard inside are requested. These points should be as close to the PCBs as possible yet still a few millimetres away from them to prevent the effects of possible glue overflowing from under the PCBs. These points will be used to define the $z = 0$ reference plane.[16]

Then the height of the hybrids and powerboard should be defined. For the hybrids, four measure points on the bond pads around each ABCStar and HCCStar chip are required, which are shown as the yellow squares in Fig.2.9. For the powerboards, four points on the data/power pads and on the powerboard-to-hybrid power pads are required, while for the fiducial mark near the HV-mux (PB_2) and the pad by the shielding shell (PB_5), one measure point is required. Detailed measurement process will be discussed in Sec.4.3.[16]

Chapter 3

Apparatus

Several instruments are used to validate and design the metrology routine via a SmartScope.

3.1 SmartScope

The SmartScope is a 3D multisensor measurement system manufactured by Optical Gaging Products (OGP), the major part of which is a telecentric $10 : 1$ zoom lens with a precise moving system. A touch probe can be and was used for the measurement. A set of lights beneath the glass table, around and in the lens can be tuned for a proper light setting.

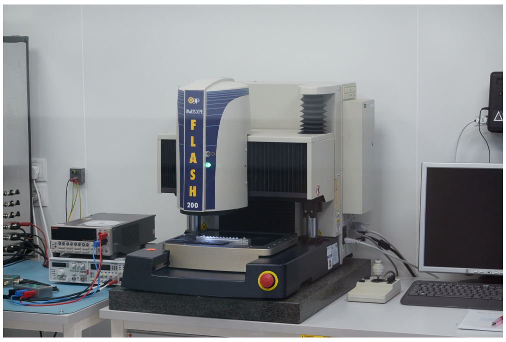

Figure 3.1: The SmartScope Flash 200 in NBI, KU.

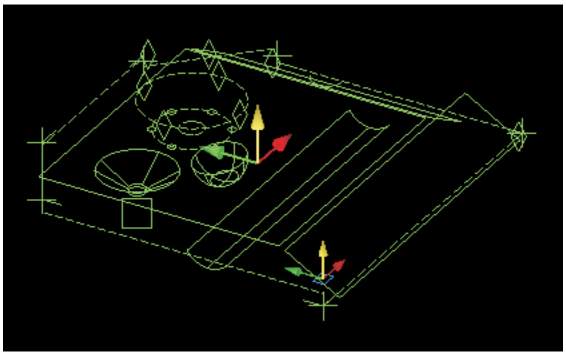

Figure 3.2: The coordinate system of the SmartScope software. Note the view origin in the middle and the part origin at the corner.[17]

The SmartScope is controlled by a specific corresponding software. A Machine Coordinate System exist in the software as the base coordinate system, while an explicit coordinate system can be set up during the measurement, known as the Set-Zero Coordinate System. There's also a Part Coordinate System available if multiple parts that are same.[18] Fig.3.2 shows an example, where the yellow arrow represents the Z-axis while the red and green arrows define the XY-plane.

At Lund University (LU), a SmartScope Vantage 250 is installed, while the installed model is SmartScope Flash 200 in Niels Bohr Institute (NBI) at Copenhagen University (KU) and in Uppsala University (UU). The differences will be discussed in the next subsection.

The telecentric lens used on the SmartScope has such a property that the magnification ratio is only affected by the focal length of the lens, and it gives an orthogonal view of the item. Thus, the off-focus objects also have the same image centre as that when in focus, which would reduce the error of the measurement. Also, the focal distance of the lens is fixed at each focal length, indicating that the lens is always at the same distance from the object, but the distance is different at each focal length setting, in another way, the zoom setting. This indicates how the SmartScope measures the height in this non-contact way. The height of the camera can be converted to the height of the object, as long as the proper zero plane is set.

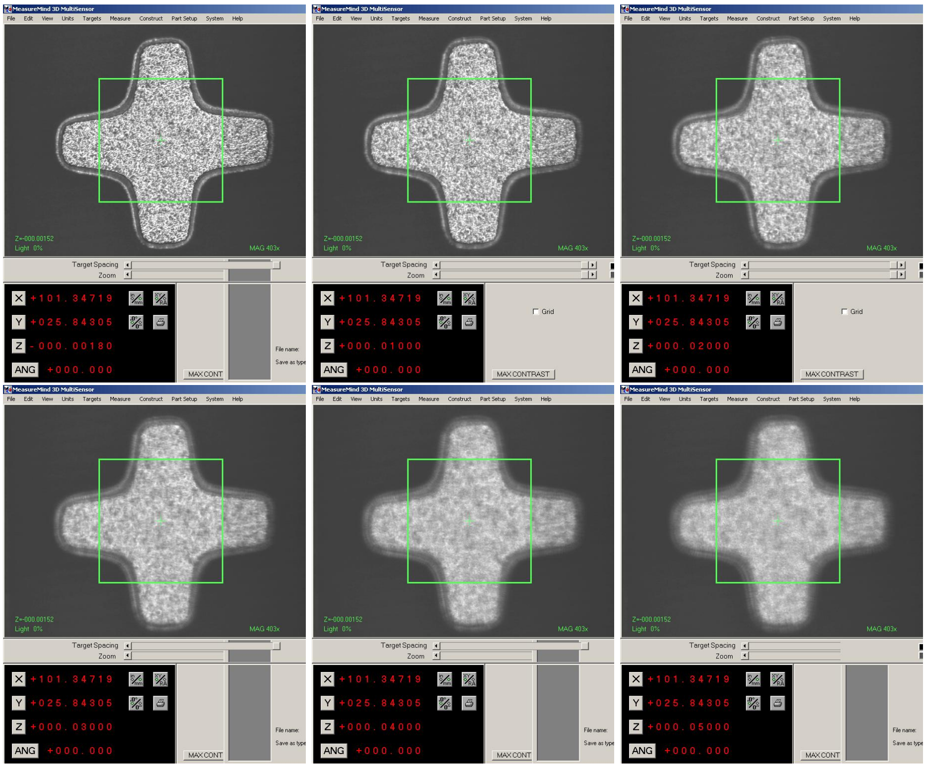

Figure 3.3: Field of view on a fiducial mark, from on-focus-height to 50 μm above the on-focus-height. The step between neighbouring pictures from left to right is 10 μm each.

One question still remains, as the machine has to know when it is in focus. This is done when the desired region reaches maximum contrast. The SmartScope will move the whole optics up and down and record the height when it reaches the maximum contrast, and beep to notify when failing to find the position. The contrast is distance-sensitive as a small offset would bring the loss of contrast, which can be shown in Fig.3.3 and Fig.3.4. Here we can see that the contract loss is visible even only with a difference of 10 µm.

The measurement on the on-sensor XY plane is much easier. The table and camera will have relative movement, which is controlled by the DC servo. The precision of the movement is at the magnitude of 1 µs. The SmartScope has multiple functions like tracing the edges, but all of the measurement is based on the fact that the SmartScope can pick up a point with a precise coordinate. For most of the time, the SmartScope would be asked to pick up a point on an edge, which could be a dividing line of two different materials like the bare copper on a PCB, or an physical edge of an item like the outermost edge of the silicon sensor.

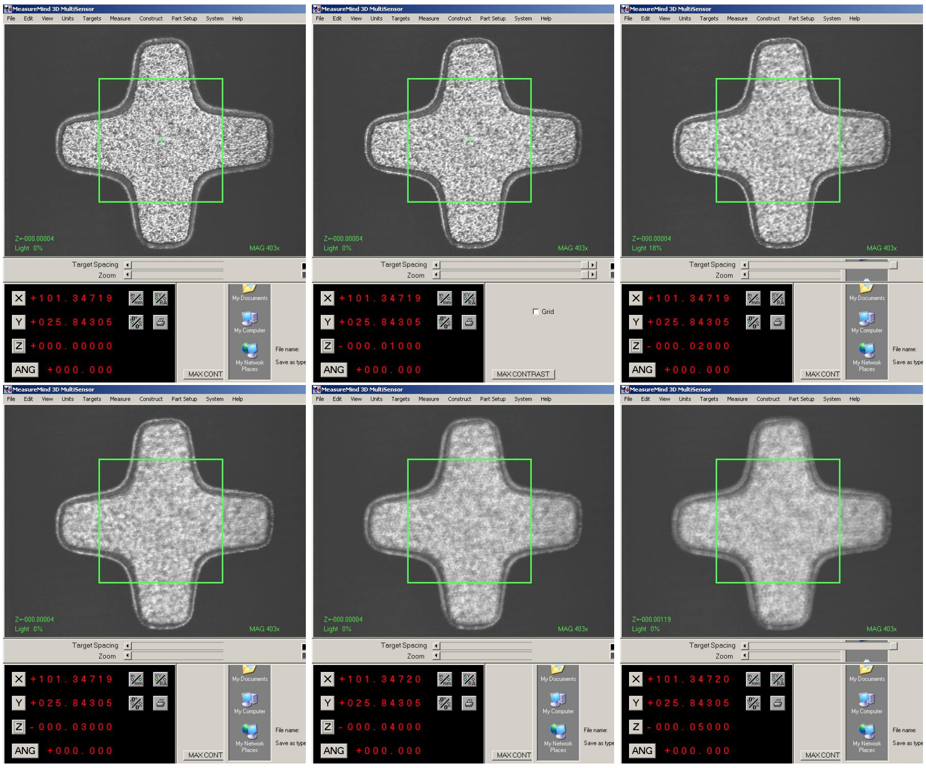

Figure 3.4: Field of view on a fiducial mark, from on-focus-height to 50 µm beneath the on-focus-height. The step between neighbouring pictures from left to right is 10 µm each.

The touch probe, however, measures the surface height with direct contact. A Renishaw Probe Interface 200 (PI200) is used to operate the TP20 touch probe. A small deflection of the stylus tip produces a force which is applied via the stylus module and kinematic coupling to the strain sensing structure housed in the probe body.[19] The level signal from the stylus will be processed, and the SmartScope system can trigger the data acquisition by such signal.

3.1.1 Differences of devices in institutes

As the metrology test will be conducted with the Flash 200 SmartScope in UU, the method and routine created and validated with the Vantage 250 in LU shall be implemented. Also, the difference between these two models should be discussed.

The most straightforward difference between the two machines is that the camera module on the Vantage 250 only moves along the height Z-axis, while the one on Flash 200 is also responsible for the X-axis measurement. That is to say, the moving table of the Vantage 250 has two degrees of freedom, while the Flash 200 only has one. This is no huge difference since the software only cares about the relative movement between the camera and the table. A minor difference could be that the unidirectional moving table would have less impact on the accuracy of the object's position, which can be dismissed as long as the object is fixed.

Other differences are more about technical specifications. The two models have a slightly different XYZ moving range, but both are sufficient for this sensor measurement ($300 \times 150 \times 200$ mm for Vantage 250 and $200 \times 200 \times 150$ mm for Flash 200). Both have an XYZ scale resolution of 0.1 µm, but the accuracy differs.[20][21]

The SmartScope Vantage 250 has an XY area accuracy of $E_2 = (1.8 + 4L/1000)$ µm, while that for Flash 200 is $E_2 = (2.0 + 6L/1000)$ µm. The Z linear accuracy for the Vantage 250 is $E_1 = (2.5 + 5L/1000)$ µm and that for Flash 200 is $E_1 = (3.5 + 6L/1000)$ µm. Note that L is the measured length in millimetres, and it indicates that the expected accuracy should be better than 4.4 µm in general. This is more than one magnitude better than the range requirement on the CERN document.[16]

3.1.2 Lighting

Both SmartScopes are equipped with three lights. The light under the glass table is for a bright background and is not used in this project. A ring light with 3×8 segments and a through-the-lens (TTL) light is of more importance here. Multiple materials are involved in the metrology test for the sensor: silicon strips, metal bonding pads, ASICs, etc. These things are never perfect reflective surfaces, and a proper light setting is significant for the best contrast.

As shown in Fig.3.5-3.8, the TTL lights will only highlight the surface structure that is perpendicular to the optical axis, and thus are harsh on the measured item. The ring-light, however, has a non-zero angle of incidence, making it easier to illuminate the edges, which will make it much easier for the SmartScope to define the edge. Yet since the field of view is

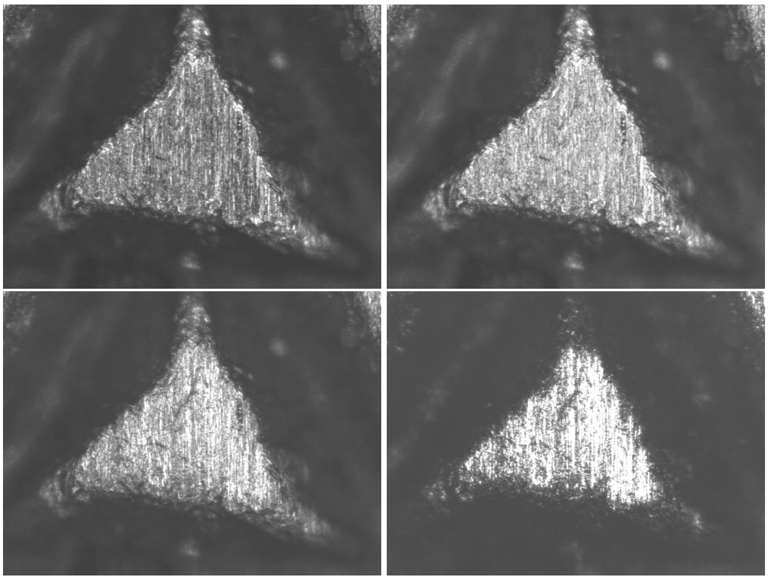

Figure 3.5: Different light configurations on the #50 block. The focused area is in a carved letter "A". Light configuration: left-up: TTL off, ring-light 60%; right-up: TTL 50%, ring-light 60%; left-down: TTL 70%, ring-light 50%; right-down: TTL 90%, ring-light off.

around 0.3×0.4 mm, this difference in the edge positioning on XY plane can be dismissed, and all it matters is the height definition.

Also, Fig.3.5 and Fig.3.6 show the situation for machined metal surfaces, Fig.3.7 shows metal bonding pad on PCB and Fig.3.8 shows the surface of the silicon strip sensor. From them it is clear that different materials will have a completely different reaction to the same light configuration. The flat, glossy PCB surface appears dark under the ring-light, and the silicon sensor will show the crystal texture on the same occasion, and the rough metal parts are always bright on any occasion.

It is important to create a high contrast view to make the SmartScope easier to focus on, and to maintain the same light configuration during the whole measurement and among different measurements to acquire a set of results that can be compared, for a different light configuration can possibly result in a different height measured.

3.2 Gauge Blocks

A few metal gauge blocks are used to validate the measurement in this project. All of the gauge blocks are chosen from one set of blocks of C.E.Johansson AB. #4, #5, #10, #11, and #50 of this set are used, and the number of each block indicates the length of the measurement

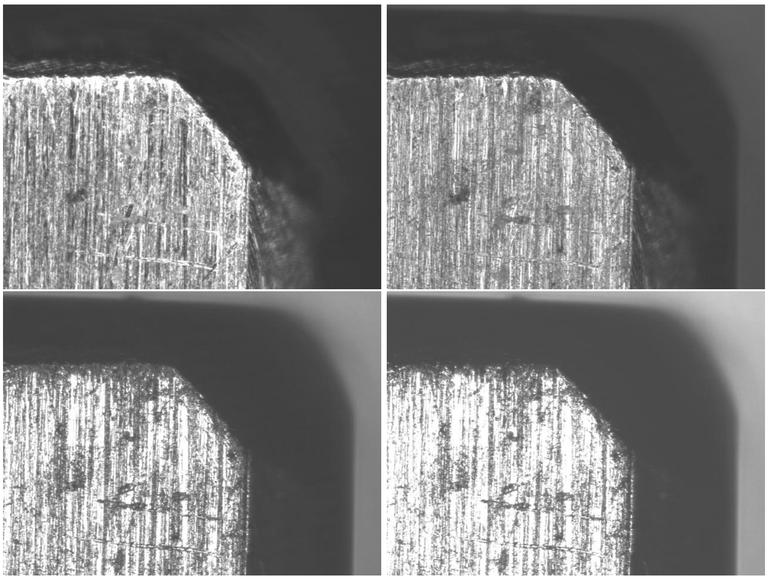

Figure 3.6: Different light configurations on the #50 block. The focused area is on the corner of it. Light configuration: left-up: TTL off, ring-light 60%; right-up: TTL 60%, ring-light 50%; left-down: TTL 80%, ring-light 20%; right-down: TTL 90%, ring-light off.

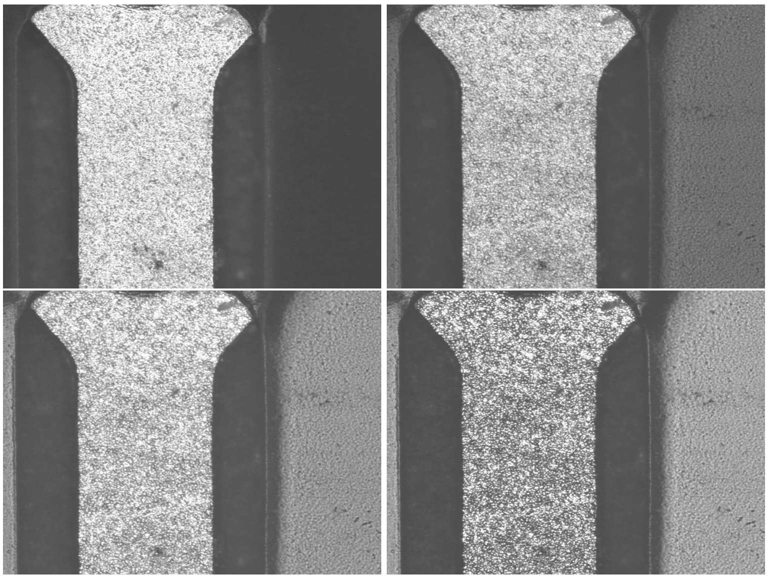

Figure 3.7: Different light configurations on a dummy hybrid. The focused area is on a metal pad. Light configuration: left-up: TTL off, ring-light 60%; right-up: TTL 70%, ring-light 50%; left-down: TTL 80%, ring-light 40%; right-down: TTL 90%, ring-light off.

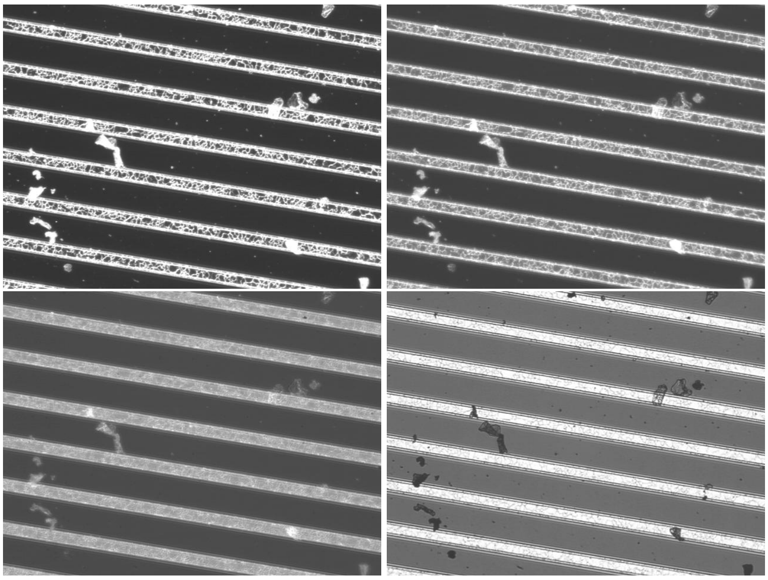

Figure 3.8: Different light configurations on a sample silicon sensor from Hamamatsu. Light configuration: left-up: TTL off, ring-light 80%; right-up: TTL 30%, ring-light 70%; left-down: TTL 40%, ring-light 60%; right-down: TTL 50%, ring-light off.

edge of each in millimetres.

However, the machining can never be perfect, so a few measurements are done to validate the actual size. Also, it is worth noticing that, the #50 block is only used as an anvil to put other blocks on.

No.	Caliper	Touch Probe
#4	4.000 mm	(3.9997 ± 0.0096) mm
#5	5.000 mm	(4.9977 ± 0.0046) mm
#10	10.000 mm	N/A
#11	11.003 mm	N/A

3.3 Mock-up of Sensor

A glass-based dummy sensor was used as the replacement before the prototype module arrived in Lund, and Fig.3.9 is the photo of it. The silicon sensor was represented by a piece of flat glass, and the hybrids and powerboard did not function. Among the two hybrids, one has true PCB but still no ASICs or wire bonds mounted. The rest two fake electronics are built with plastic, with several parts 3D-printed to resemble the geometric limits, i.e. the tallest shielding shell on the powerboard.

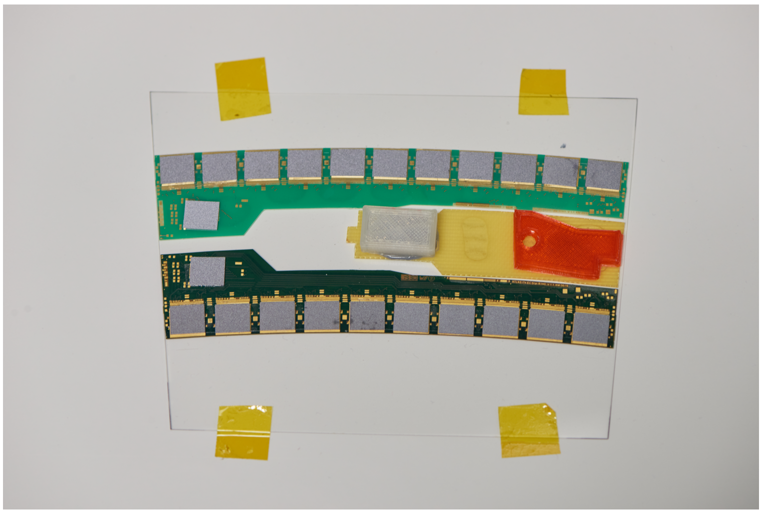

Figure 3.9: The $R0$ glass mock-up in Lund.

The idea of this glass mock-up is to provide a cheap and low-risk item to test and validate the measurement routine, as the fragile silicon module should always be measured with no coverage, which could expose the sensor to the threat of dust and other mechanical damage.

As the glass has the same shape and the one fake hybrid PCB is built with all of the necessary fiducial marks, it is possible to test the methods to measure them. However, the edges of this mock-up are full of breakages due to the property of the glass, which can be seen in Fig.3.10 and makes it difficult to define the actual edges for the mock-up. Since all measurements rely on edge measurement, this defect prevents any practical full routine from happening.

3.4 Specific Modules Used

The routine is planned to be conducted on two true modules separately, firstly at UU and then at LU. The sensor used at LU is an $R0$ PPA (Pre-Production A) and is shown in Fig.3.11, with the serial number 20USEM00000044, while the one at UU is an R1 and shown in Fig.3.12, which is also a PPA model with the serial number 20USEM10000014. However, by now only the R1 at UU was tested.

The $R1$ PPA module was tested and measured at UU. It went through the electronic and thermal tests, and when it was tested with the protect frame on a vacuum plate, the acrylic cover was adsorbed down and squashed the shielding box on the powerboard, which can be clearly shown in Fig.3.13. Also, the pink foam for buffering and protecting was put above the silicon part, and the result can be clearly told from the colour difference on the exposed silicon parts.

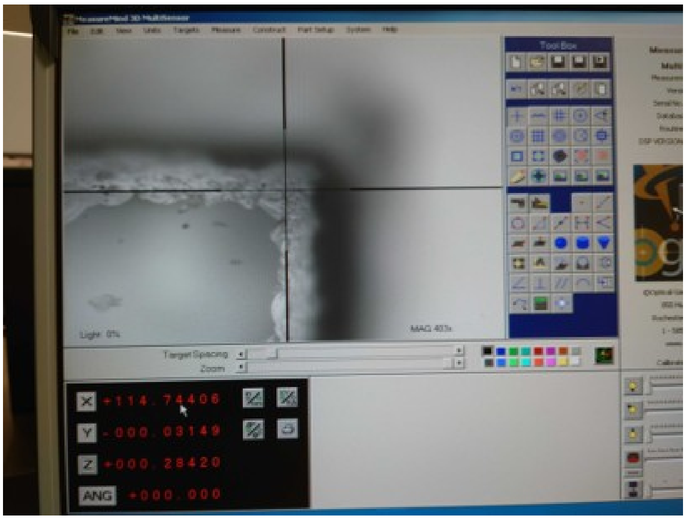

Figure 3.10: A corner of the $R0$ glass mock-up at LU. The cracked edges are clearly shown.

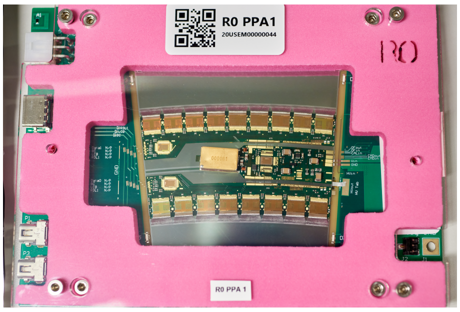

Figure 3.11: The $R0$ PPA module tested at LU on its arrival day.

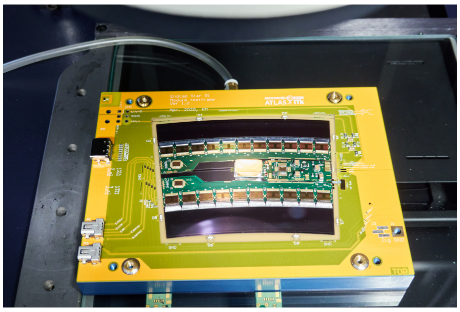

Figure 3.12: The $R1$ PPA module tested at UU.

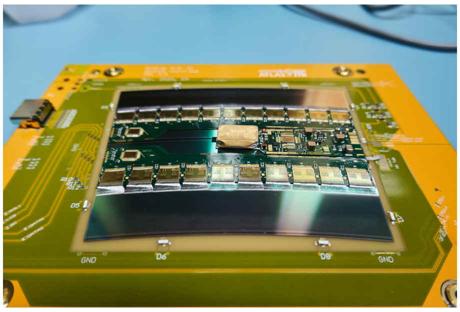

Figure 3.13: The $R1$ PPA module tested at UU.

This sample went through a few metrology tests during the author's visit to UU in 2023 March. The fiducial marks were measured multiple times to check the consistency of the measurement, as was the height measurement. Also, a full routine was created and conducted multiple times to validate the consistency when the position of the sensor was moved.

During the metrology test, the acrylic cover and foam should be removed, and the sensor was moved alongside the testing frame, which is the yellow circuit board beneath and can be seen in Fig.3.12. The frame should be put on a jig, which is a chunk of metal with trenches and holes for vacuum adsorption. To improve the precision of the measurement, the testing frame should always be adsorbed by a vacuum pump, in which way enough friction can be provided to prevent the frame or the sensor from any displacement.

The measurement for the $R0$ PPA module should follow the same principles, and there is no fundamental difference between the metrology test at UU on the $R1$ PPA and that at LU on the $R0$ PPA. The differences only appear in the fact that the shield box of the LU $R0$ is still undamaged, leaving more things to measure, and the different geometry between the two modules and consequently a different number of ABCStars.

Chapter 4

Methods

In this chapter, the complete measurement process will be discussed in details. The procedure is based on the CERN document AT2-IS-EP-0067 and is updated based on the latest decisions from the collaboration.[15][16]

4.1 Coordinate System Setting

The whole measurement should have a coordinate system as a reference for all measurements. The coordinate system is based on the silicon sensor. Fig.4.1 shows the idea of the coordinate system. The endcap sensors themselves have fan shapes. Thus, it is impossible to appoint an edge to be the axis. Thus, the upper left corner is appointed as the zero point, while the upper right corner is the point to define the X-axis. The $z = 0$ plane is defined additionally by the lower left corner. As a Cartesian coordinate system is always used here, the Y-axis will be naturally derived. Note that for endcap modules, this third point is never on the Y-axis as the artificial edges are not perpendicular, which is clear in Fig.4.1. In this way, the coordinate system is decided.

However, in practice, it is not necessarily that the edge corners are chosen as the reference point. The sensor is designed with a safety outer ring, the slight damage of which doesn't affect the performance of the whole sensor. Thus features slightly inside can be chosen as the reference point, and all the positions can be moved correspondingly afterwards. In this project, the HV-ring is chosen as the feature, for 1) this ring is printed on the silicon and represents the true position of the silicon segments; 2) it is much clearer to define; 3) the sensor could work when the part outside the ring is broken but hardly when inside.

In actual measurement, the sensor is always fixed. As a fragile unit, it should be transported and tested on a test frame as shown in Fig.4.2. During the metrology test and other manufacturing processes, the module is always put on a jig, which is a metal chunk with small

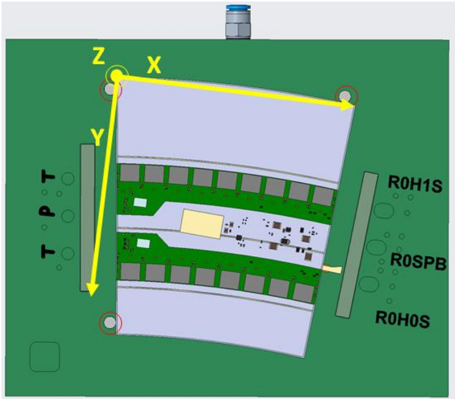

Figure 4.1: Example of an endcap module on an assembly jig with coordinate system highlighted in yellow.[16]

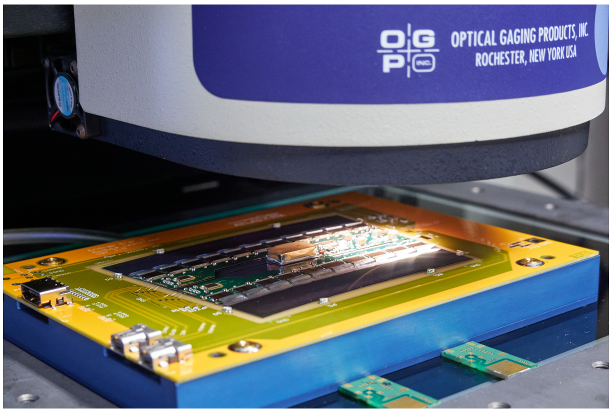

Figure 4.2: A sensor on a test frame, while the frame is on a jig.

holes for vacuum adsorption, with parts that can constrain the sensor. In this way, the sensor or frame can be fixed without any potential damage, just like what is shown in Fig.4.2.

4.2 XY-plane Measurements

The measurement of the hybrid and powerboard positions on the sensor plane is straightforward, as the SmartScope is designed to measure with optical tools most of the time. On the plane, the parts have three degrees of freedom (X, Y and rotation); thus, at least two points each are used to define the hybrid and powerboard.

4.2.1 Hybrid

As shown in Fig.4.3, the position of a hybrid is defined by two outermost fiducial marks, which are named H_X_P1 and H_X_P2. Fig.4.5 shows a typical fiducial mark, which is printed on the PCB and has a special shape, so that it can be easily and precisely identified.

The cross-fiducial has an area, and the position of this fiducial mark is defined by the centre of it. A typical fiducial mark of this kind is shown in Fig.4.5. However, the positioning of the fiducial marks requires additional processes, for the edges of them are not necessarily straight due to manufacturing reasons.

Two methods can be applied to define the centre. The first one can be applied when the four tips of this cross-shaped fiducial are round. The SmartScope software has the function to

Figure 4.3: Barrel hybrid with fiducials for position measurements highlighted in yellow.[16]

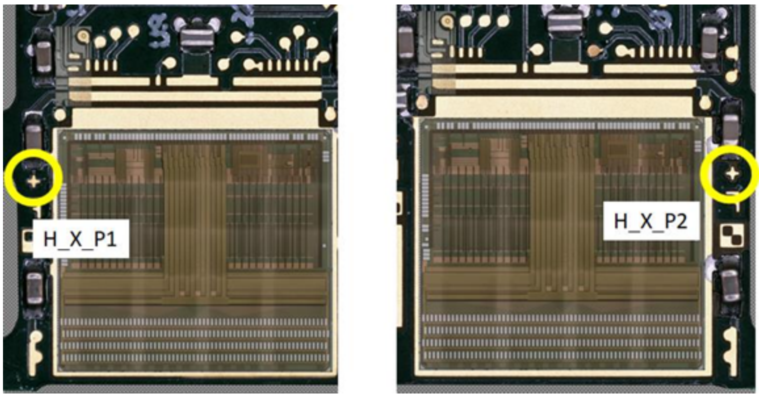

Figure 4.4: Example for naming of the points, as described in hybrid metrology document.[16]

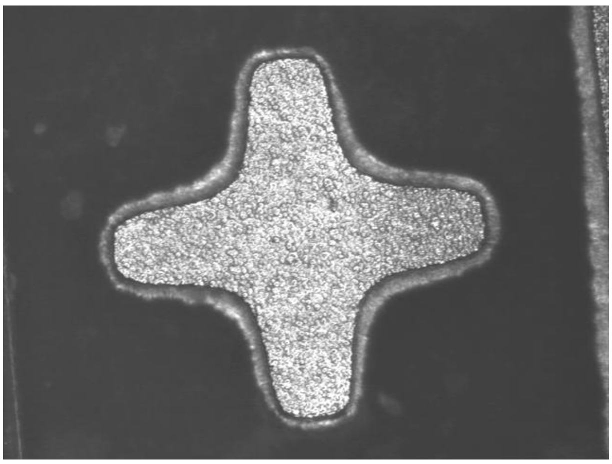

Figure 4.5: One cross-fiducial under SmartScope. Note that the width of this fiducial is about 0.3 mm.

define a circle based on three measured points; thus, a point within each tip can be measured when the tip is fitted as a circle. Finally, the centre can be defined by the intersection of the lines connecting opposite points.

This method runs quickly with only four measurements; however, the fiducial doesn't always have round tips. A more general method can be applied where the straight edges are measured.

In this method, two side edges of each tip are measured; thus, there are a total of eight points measured for the four tips. Four lines are created accordingly to form two sets of lines roughly parallel, which gives four intersections that can form a convex quadrilateral.

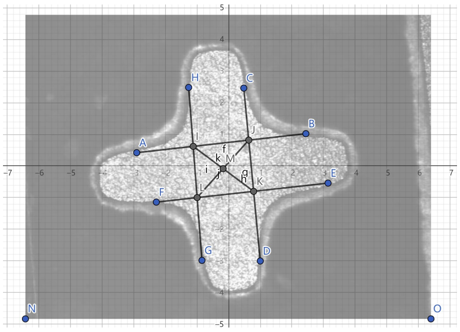

Figure 4.6: The cross-fiducial with virtual measurements via Geogebra online.

Fig.4.6 gives an illustration of this method. This method shows strong reproducibility, as the inner quadrilateral will not exceed the fiducial, and the centre point to define its position will always be somewhere in the middle. As described in Sec.2.2, the XY allowance is ± 0.25 mm, while the uncertainty brought by this method will be far less than 0.1 mm, which is about the size of the centre region.

The process to guarantee that the fiducial falls within the allowance will be discussed in Chap.5.

4.2.2 Powerboard

Similarly, the position of each end-cap powerboard is defined by two double-square shape markers, which can be seen in Fig.4.7. A few of them can be found in the photo, yet two are appointed for the position measurement. The definition of this fiducial marks is simpler than the one on the hybrids, as only four points will be picked on two edges in the middle, and the centre is defined as the intersection of the two lines created from the opposite points.

For the barrel powerboards, two holes are used for the position definition, yet the barrel sensor metrology is not included in this project.

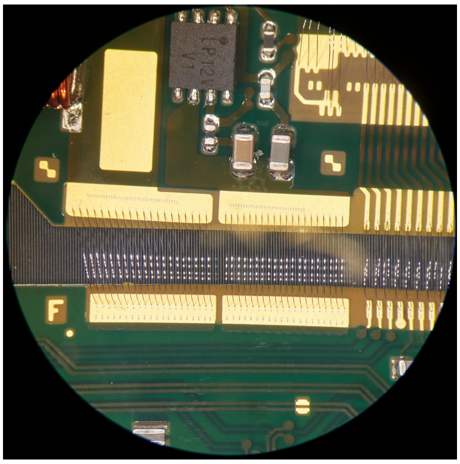

Figure 4.7: The lower part of the $R0$ powerboard and upper of the $R0$ hybrid H0.

4.3 Height Measurements

The height measurement is the most complex task in the whole metrology test, as the SmartScope relies on the movement of the camera to give the height. As discussed in Sec.3.1, the SmartScope has the ability to find the focal point by seeking the highest contrast of the image, which is less direct than the XY measurement. However, the height measurement reveals the glue thickness between the electronics and the sensor, which affects the heat conductance and could cause possible collisions between modules as they are densely populated.

4.3.1 Sensor

It is important to set up a zero plane when a height measurement is conducted, and the upper surface of the silicon sensor is the ideal one with sufficient patterns on it. Another practical reason is that the glue sits between the PCBs and the sensor and the glue shall be avoided in all measurements.

To measure the sensor, a series of points are taken for this task. In principle, more than four points that create a square that contains the hybrids and powerboard as much as possible should be used, yet in practice, many more points with a uniform distance can be chosen, as it would always be better to have more than four points to fit the plane.[16] In a test routine conducted at Uppsala University with an $R1$ model, 21 points are used, with 11 on the wider side and 10 on the narrower side. These points can reduce the uncertainties of the sensor plane measurement and reflect the flatness of the silicon. This test run will be discussed in Chap.5.

The procedure guideline also recommends that the points chosen are taken a few millimetres away from the PCBs yet still close to them. In the Uppsala test routine, the points are approximately 1 mm from the two hybrids, with no points taken between hybrids and powerboards, for the glue could be on this part of the sensor and bring errors, as said in the the operation document.[16]

4.3.2 Hybrid

Exposed metal pads on the hybrid PCB **have** to be used for the surface height measurement. A few patterns are required.[16]

1. The copper pads by the ABCStar chips, which are the "F" and cross fiducials shown in Fig.4.8. At least four points should be taken, and they are named as ABC_RxHy_n.
2. The four copper pads around the HCCStar chips, which are shown in Fig.4.9. At least four points should be taken, and they are named as HCC_RxHy_n.
3. Two measurements near the stave/petal data pads near the HCC, which are shown as the leftmost golden bonding pads in Fig.4.9.
4. The hybrid-to-PB power pads, which are shown in Fig4.10-4.11.
5. The large square pad at the far end of the hybrid from the HCC.

These patterns are measured by sequence and analysed in the post-processing program.

4.3.3 Powerboard

The powerboard does not have so many ASICs like the hybrids with ABCStar and HCCStar, yet there still exists a list of all of the things to measure:

1. PB_1 is the averages the four points taken on the data/power pads on the left.
2. PB_2 is the single point on the fiducial near the HV-mux.
3. PB_3 is the average of the four measurements on the top PB-to-hybrid power pads.
4. PB_4 is the average of the four measurements on the bottom PB-to-hybrid power pads.
5. PB_5 is the single point on the tab to the very right.
6. All measurements on the capacitors ($C1, C2, C3, C4$) should be reported individually.

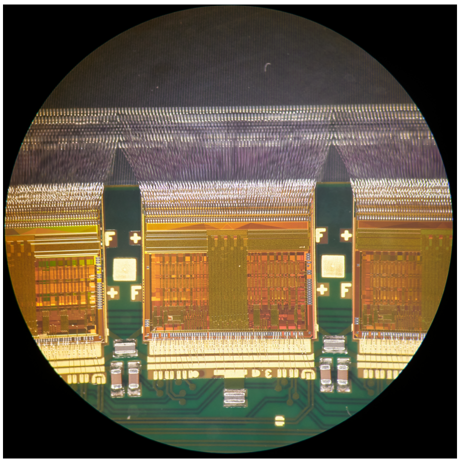

Figure 4.8: $R0$ under microscope with a few ABCStars in view. Note the fiducial marks in the between.

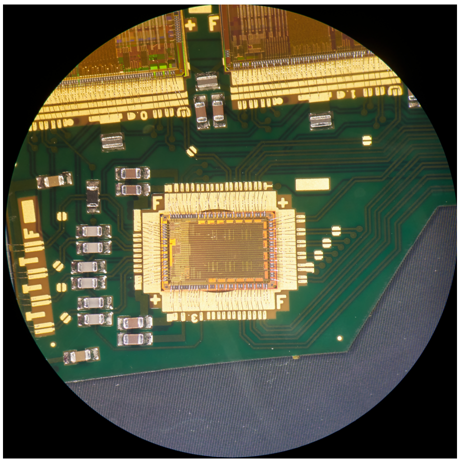

Figure 4.9: $R0$ under microscope with an HCCStar in view. Note the four fiducial marks on the corner of the HCC.

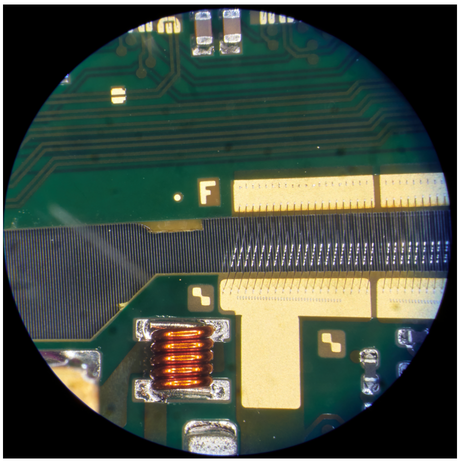

Figure 4.10: $R0$ under microscope with $R0H0$ and powerboard in view. This is the bonding area between the hybrid (up) and powerboard (down).

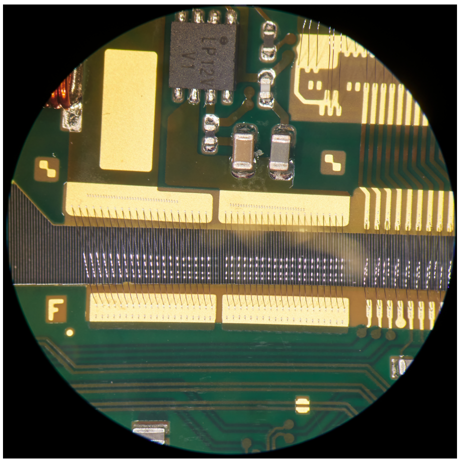

Figure 4.11: $R0$ under microscope with $R0H1$ and powerboard in view. This is the bonding area between the hybrid (down) and powerboard (up).

7. The five measurements on the shield box (Shield) should be combined into a single number which is the maximum of the five.

These patterns are measured in sequence and processed in the analysis program.

In the routine conducted in Uppsala, the capacitors and shield box are excluded. The shield box was pressed and cracked, so it was meaningless to measure it.

4.4 Analysis Program

Given the complexity of the measurement, a post-processing program is necessary, even with the calculated results from the SmartScope software. This program aims to solve the following tasks:

1. To read the measurement from the SmartScope output file.
2. To calculate necessary results.
3. To create an output file in the required format.
4. To illustrate the measurement in a interactive graphical interface when necessary.

The last illustration is not part of the measurement task so it was handled separately. A C++ program package was developed to fulfil the rest functions, for the customized classes and functions can easily handle the different measurements.

After testing with several iterations, the program can now read the SmartScope output file with different data sets collected at LU, UU and NBI, as the output formats depend on the setting of the local SmartScope software. The files are organized by lines, and each line is stored with the sequence number, the type (point, line, intersection and so on), the coordinate, the so-called size (which is the general name given to the angle between lines, the diameter of circles and other properties of different features) and the measurement reference.

The different types of measurements are organized into a few geographical classes, which can be straightforwardly achieved with C++. Based on a *point* class that only consists of an XYZ coordinate, a *point with distribution* class and a *circle* class are created. The *point with distribution* class aims to describe a point with a standard deviation, which is useful when multiple measurements on the same point are conducted. The circle class is used to describe the circle measurement from the SmartScope.

With two points, a vector class and a line class are introduced. They are supposed to be the same thing, but to make everything clear, they are separated to achieve different targets. The vector class is described by a starting point, an ending point and the vector described by XYZ coordinate. The line class is described by two points on the line and a vector to indicate the direction of the line. The actual length of the line is arbitrary and can be normalized for easier calculation.

One more important class introduced is the plane class. This plane class is only described by a point on the plane and the normal vector of the plane.

All of the above classes are used for different functions. Basic calculation of trigonometric functions is achieved with simple vector calculation. With that, the distance between different items can be realized. The distance between two points and between one point and one plane is easy to calculate, while the one between one point and one line costs a few more steps.

As described in Sec.4.2.1, the cross-fiducial requires taking intersections of lines, and such a calculation is very common during post-processing. However, a problem arises naturally. The lines are almost never strictly coplanar and have no mathematical intersection because measurement errors from SmartScope and calculation errors from computer float numbers exist. Thus, the definition of the line intersection here is the midpoint of the shortest line segment between two lines. The only interesting intersection is between lines, as the *plane* is only used to calculate the height difference, and no intersection calculation is involved with planes.

One more function derives a plane from multiple points. The plane is fitted with linear least squares. Singular value decomposition is used to calculate the result, for there exists a linear algebra package named *Eigen* that can solve the result quickly, and SVD can give a relatively good result.[22]

Finally, the results are organized and output in the format required. A sample can be seen in Fig.4.12. The comparison between the results and the schematic of the module, Fig.4.13-4.14 showed a valid and reasonable result.

The code is uploaded to a GitHub project under the thesis name.[23]

4.5 Validation with the Gauge Blocks

Before testing this method on the sample sensor, the SmartScope routine and an earlier version of the post-processing program were tested on a few gauge blocks, which are metal blocks that have precise widths on one side. The marking of the block is the width in millimetres.

As described in Sec.3.1, NBI and UU share the same model of the SmartScope, while there is another model at LU. So it is necessary to validate the consistency of the machines.

#10 and #11 blocks were measured at NBI and LU. As the calculated edges are not exactly parallel, the distances between neighbouring corner points are used. The result showed that the differences are all better than 0.15%, and most of them are better than 0.06%.

Another test is to validate the accuracy of the SmartScope. A comparison between optical SmartScope and physical probe results is conducted on #4 and #5 blocks. The blocks are put in a way that the number of them indicates the height in millimetres. They were put on a #50

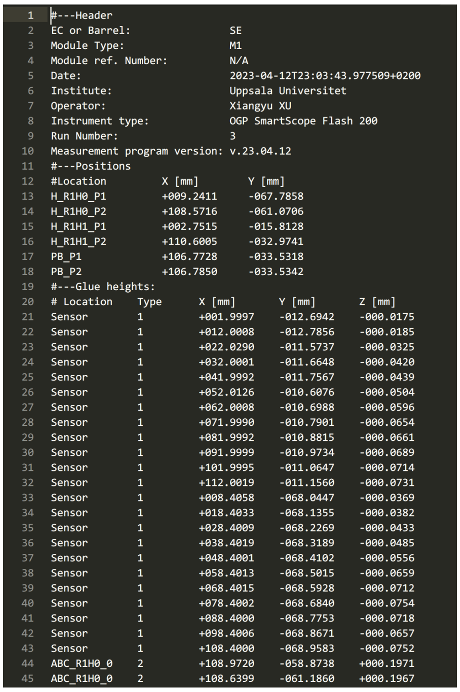

```
#---Header
EC or Barrel:               SE
Module Type:                M1
Module ref. Number:         N/A
Date:                       2023-04-12T23:03:43.977509+0200
Institute:                  Uppsala Universitet
Operator:                   Xiangyu XU
Instrument type:            OGP SmartScope Flash 200
Run Number:                 3
Measurement program version: v.23.04.12
#---Positions
#Location        X [mm]       Y [mm]
H_R1H0_P1        +009.2411    -067.7858
H_R1H0_P2        +108.5716    -061.0706
H_R1H1_P1        +002.7515    -015.8128
H_R1H1_P2        +110.6005    -032.9741
PB_P1            +106.7728    -033.5318
PB_P2            +106.7850    -033.5342
#---Glue heights:
# Location    Type      X [mm]       Y [mm]       Z [mm]
Sensor        1         +001.9997    -012.6942    -000.0175
Sensor        1         +012.0008    -012.7856    -000.0185
Sensor        1         +022.0290    -011.5737    -000.0325
Sensor        1         +032.0001    -011.6648    -000.0420
Sensor        1         +041.9992    -011.7567    -000.0439
Sensor        1         +052.0126    -010.6076    -000.0504
Sensor        1         +062.0008    -010.6988    -000.0596
Sensor        1         +071.9990    -010.7901    -000.0654
Sensor        1         +081.9992    -010.8815    -000.0661
Sensor        1         +091.9999    -010.9734    -000.0689
Sensor        1         +101.9995    -011.0647    -000.0714
Sensor        1         +112.0019    -011.1560    -000.0731
Sensor        1         +008.4058    -068.0447    -000.0369
Sensor        1         +018.4033    -068.1355    -000.0382
Sensor        1         +028.4009    -068.2269    -000.0433
Sensor        1         +038.4019    -068.3189    -000.0485
Sensor        1         +048.4001    -068.4102    -000.0556
Sensor        1         +058.4013    -068.5015    -000.0659
Sensor        1         +068.4015    -068.5928    -000.0712
Sensor        1         +078.4002    -068.6840    -000.0754
Sensor        1         +088.4000    -068.7753    -000.0718
Sensor        1         +098.4006    -068.8671    -000.0657
Sensor        1         +108.4000    -068.9583    -000.0752
ABC_R1H0_0    2         +108.9720    -058.8738    +000.1971
ABC_R1H0_0    2         +108.6399    -061.1860    +000.1967
```

Figure 4.12: A sample of the output from the program. This result was obtained from a $R1$ sample module in Uppsala University.

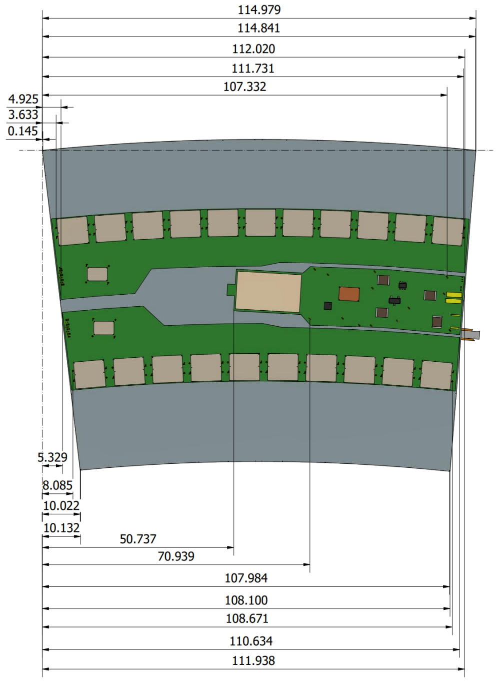

Figure 4.13: The schematic of the $R1$.

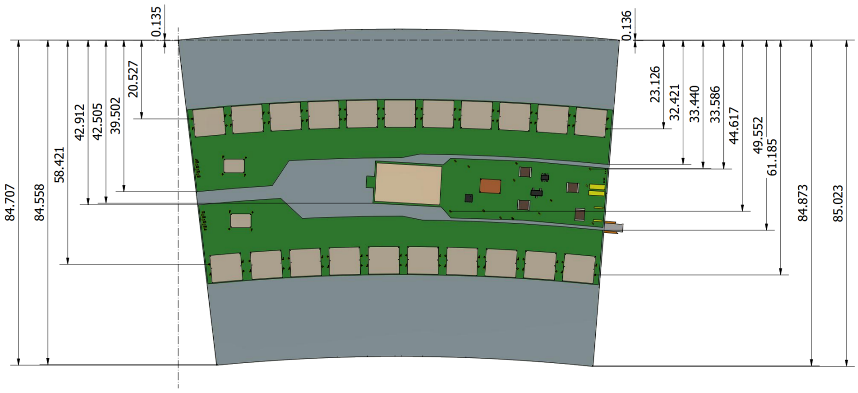

Figure 4.14: The schematic of the $R1$.

block.

The planes were all fitted with the linear least squares method introduced in Sec.4.4. All of the normal vectors calculated were rather perpendicular to $z = 0$ plane; the X component and Y component of the normalized normal vector are better than 6×10^{-4} rad away from the vertical line. The standard deviations for this probe measurement are better than 0.04 mm. For the optical SmartScope measurement, the X component and Y component of the normalized normal vector are better than 4×10^{-3} rad away from the vertical line. The standard deviations for this are better than 0.04 mm. The height differences are relatively 1.478% and 1.568% and are better than 0.08 mm.

As it is suspected that this error comes from the gap between the two blocks, an additional test was done on several one-piece metal parts. The results showed a similar systematic difference between the optic and touch probe methods, which is a few dozen micrometers. By now there is not enough evidence to determine what caused this difference.

Chapter 5

Results

With the post-process program, the measured points can be turned into meaningful sizes or positions of the items. To validate this result, a few measurements were conducted on the mock-up sensor dummy and the gauge blocks. The tests on the mock-up at LU verified the accuracy of this method, and the tests on the gauge blocks proved the consistency among different SmartScopes. A routine was made and tested on an $R1$ pre-production prototype, and three individual results were gained at UU. Such results proved the consistency of this system, yet a few challenges arose as we gained the result.

5.1 Mock-up Measurements

With the mock-up module, it is possible to test the fiducial measurement and other validations.

The first test was to validate the post-process program. A few items were measured on the mock-up, and the SmartScope provided simple but necessary tools to calculate certain intersections. The same calculation with the post-process program returned the result with relative differences better than 0.01%.

The second test was to validate the fiducial measurement. Three fiducial marks were measured separately four times, and their corresponding standard deviation on the XY plane was 0.00213 mm, 0.00306 mm and 0.00124 mm, which is good enough for the sensor measurement, since the criteria require both absolute values of ΔX and ΔY smaller than 0.25 mm.

5.2 Gauge Block Measurements

A few measurements were conducted on the gauge blocks to verify the performance of the SmartScope and the corresponding software. It is vital to validate the results of this machine so that the measurement on the modules could be treated.

5.2.1 Measurement Consistency

The first is to repeat the measurement of the width and length of the blocks in LU and in NBI to see if the two different machines return a consistent result. Block #10 and #11 were used. Note that this is an early test, when the light configuration was arbitrary and set to the highest edge contrast. Errors could be generated from this light difference, for the edges observed would move with a change of the light configuration.

The width and length were defined by the distance between four corners of the upper surface of the block, for the measured opposite edges were not necessarily parallel, resulting in an undefined distance between two edges. The corners were defined by the intersection of the two edges on which the corner was located, and each edge was defined by two points on it, for the SmartScope mostly measures a point on an edge, as discussed in Sec.3.1. Fig.3.5-3.8 clearly showed the difference, and the field of view is about 0.3 mm $\times$ 0.4 mm.

No.	#10	#11
LU	9.7802 mm	10.847 mm
	9.7741 mm	10.847 mm
NBI	9.7910 mm	10.862 mm
	9.7879 mm	10.842 mm

Table 5.1: The width of the blocks. The reference size is the block number.

No.	#10	#11
LU	29.684 mm	34.702 mm
	29.636 mm	34.641 mm
NBI	29.690 mm	34.682 mm
	29.650 mm	34.661 mm

Table 5.2: The length of the blocks. There is no reference size.

No.	#10	#11
Width	0.110%	0.028%
	0.141%	0.046%
Length	0.020%	0.058%
	0.047%	0.058%

Table 5.3: The relative difference for this result.

The results for the width of the block are shown in Tab.5.1, and the result for the length of the block are shown in Tab.5.2. The relative difference for the same edge between results from LU and NBI is calculated and shown in Tab.5.3. It is clearly shown that the measured differences agreed with each other at the magnitude of one thousandth, and the largest difference happened on the width of the #10 block.

However, these blocks proved to be accurate by measuring them with a micrometre screw gauge. The average width is (10.000 ± 0.001) mm for #10 and (11.002 ± 0.002) mm for #11. The length of these blocks are not designed to be completely accurate, yet under a caliper #10 is 30.00 mm while #11 is 35.00 mm. It can be indicated that the measurements are $1 \sim 2\%$ smaller than the expected sizes, which could be a result of light configuration, as only the upper flat surface was illuminated and the chamfer was not included in the width measurement.

This test indicated that the two different models of the SmartScope, the Quest Vantage 250 and the Flash 200, return the results with high consistency, which is within expectation.

5.2.2 Measurement Accuracy

The second measurement involved the #4, #5 and #50 gauge blocks. This test is meant to demonstrate the accuracy of the SmartScope optical measurement. Both the camera on the machine and the touch probe are used to measure the same configuration of the gauge blocks.

The #4 and #5 were put on the #50 parallel to the shorter edge of #50, so that the upper surface of #50 can be used as the reference plane for the bottom glass table that can hardly show patterns to focus-on, which denied the possibility of taking the glass table as the reference plane as usual. In the optical test, the #50 was treated as the reference plane with four corners measured and treated in the post-processing program. An additional measurement of 16 points was done on the #50 surface between #4 and #5. The upper surfaces of #4 and #5 were also measured, with a 5×5 dot matrix measured for each. In the touch probe measurement, three 5×5 dot matrices were measured for #4, #5 and #50. Specifically, the matrix on #50 was divided into three groups: two rows on the left of #4, two on the right of #5 and one in the middle of the two.

As the dot matrices covered the whole upper surface of the blocks, it is more sensible to fit them with a plane rather than simply averaging the height, for this surface could be tilted. The average height for each column or row is also calculated. Comparing the tilt angles of the surfaces also extracted the heights. With the post-process program, it is possible to calculate the normal vector of the plane. Note that these normal vectors are all normalized. As a reference, the results from the touch probe would indicate the attitude of the blocks. The dot matrices were fitted into planes. The normalized normal vectors of the reference plane, #4 plane and #5 are $(0.00015, -0.00001, 1.00000)$, $(-0.00053, -0.00007, 1.00000)$ and $(-0.00013, -0.00001, 1.00000)$, indicating that the tilt angles were better than 4 degrees. It suggests that if this surface was approximated as the internal XY plane of the machine, the height difference caused by this angle for a 30 mm-long block would be better than 30 μm.

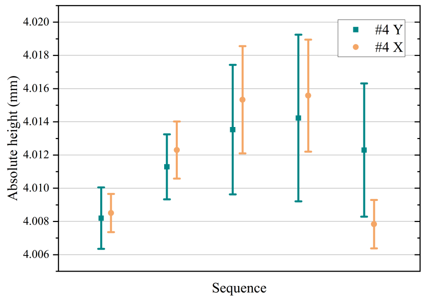

Figure 5.1: The averaged heights of #4 along two axes from touch probe measurement. The height is relative to the routine datum plane.

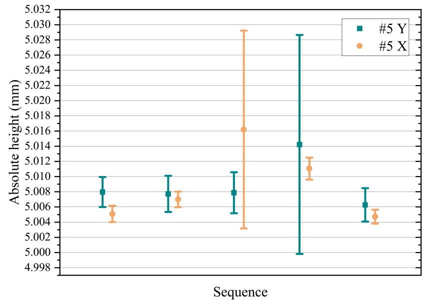

Figure 5.2: The averaged heights of #5 along two axes from touch probe measurement. The height is relative to the routine datum plane.

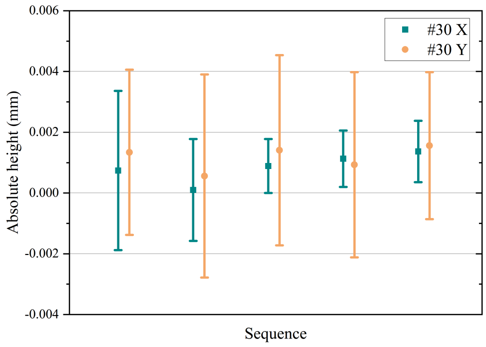

Figure 5.3: The averaged heights of #50 along two axes from touch probe measurement. The height is relative to the routine datum plane.

The planar difference is derived by taking the intersection between the plane and line $x = y = 0$. In this way, the heights for reference plane, #4 and #5 are (35.02900 ± 0.00911) mm, (38.92634 ± 0.01940) mm and (39.98960 ± 0.03652) mm. Hence the height difference can be calculated to extract the block height. #4 gauge block has (3.89734 ± 0.02143) mm and #5 has (4.96059 ± 0.03763) mm.

The separately grouped heights agreed with this uncertainty. The scale in Fig.5.1-5.3 is 2 μm, and it is obvious that certain measurements returned with a height far from the average, which should be the major contribution to the uncertainty of the height. There is no way to know if those values come from an internal error from the machine or from the uneven surface. More tests repeating this measurement shall answer this question.

With the same method, we can process the result from the optical measurement. The normalized normal vectors of the planes for #50, #4 and #5 are $(-0.00005, -0.00006, 1.00000)$, $(-0.00325, -0.00027, 0.99999)$ and $(-0.00135, 0.00012, 1.00000)$. It is clear that the tilted angle for #4 is especially large. If we take the internal machine XY plane as this surface, the resulting height error for a point 30 mm away would be 1.7 mm, which is far from acceptable. The heights for #50, #4 and #5 are (0.02757 ± 0.03489) mm, (3.98250 ± 0.00597) mm and (5.06597 ± 0.01115) mm. By reducing the height of the reference #50 plane, the block height for #4 is (3.95492 ± 0.03540) mm and that for #5 is (5.03840 ± 0.03663) mm.

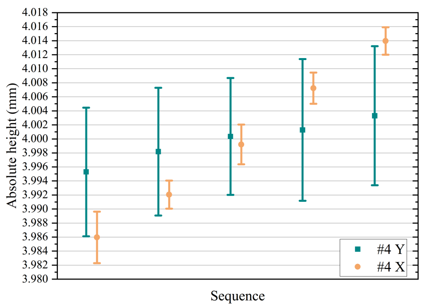

Figure 5.4: The averaged heights of #4 along two axes from optical measurement.

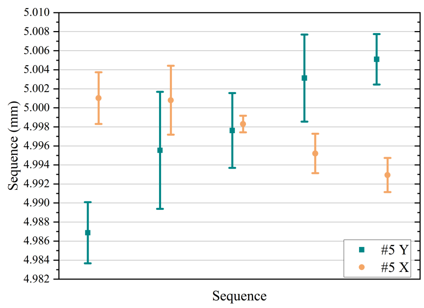

Figure 5.5: The averaged heights of #5 along two axes from optical measurement.

The results from the separated rows showed something interesting. The standard deviations of this five-point line can be as good as the one of the touch probe; however, the one from the measurement of the Y-axis had a significantly larger standard deviation. Also, both blocks showed a monotone increase or decrease of the height among both axes, indicating that the upper surfaces of both blocks have a rather large tilt angle.

The additional measurement on the single parts as shown in Fig.5.6 showed a similar result: the relative height measured from the optical method and the touch probe has a systematic difference, and no simple conclusion can be made with current experiment results.

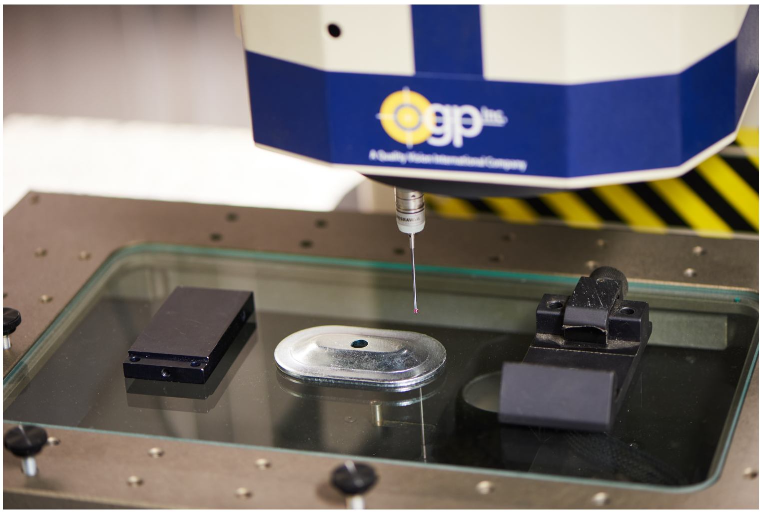

Figure 5.6: The parts under the touch probe for the accuracy validation. Parts from left to right are No.2, No.1 and No.3.

5.3 Sensor Measurements

The most important part should always be the measurement of the true sensor. The measurement has been done on one $R0$ module at LU and one $R1$ module at UU. A corresponding measuring routine has been created for each of the modules, and all of the required components were measured if possible.

The post-process program calculated the necessary positions and organized these positions into an output file under the requirements of the CERN document.[16] A sample is attached in the Appendix.

The routine at UU for the $R1$ sample was repeated three times, and gave slightly different results as the SmartScope edge finder does not always repeat the result, yet returns the result within the expected fluctuation. The distribution of the height measurement results was better than $7\ \mu\mathrm{m}$ as shown in Fig.5.7, and that of the XY distribution was better than $2.5\ \mu\mathrm{m}$, which indicates that this method is reliable and ready for real-world sensor production process.

The last step is to compare the measurement result with the standard position of the fiducials to determine if this module should pass the metrology test. The design schematic of the sensor is the standard used as reference, and an example for the $R1$ module is Fig.4.13-4.14. In the case of the third measurement, the ΔX and ΔY is shown in Tab.5.4. Note that only both ΔX for two powerboards exceeded the allowance.

The relative height of measured to the silicon plane is shown in Fig.5.8. Note that this

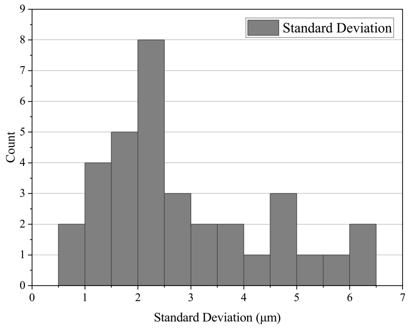

Figure 5.7: The histogram of the standard distribution of the height measurements for all the height check-points on $R1$.

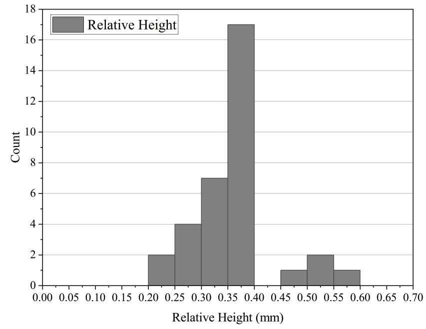

Figure 5.8: The histogram of the heights measured for all the check-points on $R1$.

height distribution is far from the $0.070\ \mathrm{mm} \sim 0.170\ \mathrm{mm}$ range, yet further measurement is required to verify if this comes from the property of this module.

Items	$\|\Delta X\| < 0.25\ \mathrm{mm}$	$\|\Delta Y\| < 0.25\ \mathrm{mm}$
H_R1H0_P1	$0.0533\ \mathrm{mm}$	$0.0741\ \mathrm{mm}$
H_R1H0_P2	$0.0963\ \mathrm{mm}$	$-0.1335\ \mathrm{mm}$
H_R1H1_P1	$0.0362\ \mathrm{mm}$	$-0.1103\ \mathrm{mm}$
H_R1H1_P2	$0.0114\ \mathrm{mm}$	$-0.1854\ \mathrm{mm}$
PB_P1	$0.2791\ \mathrm{mm}$	$0.1413\ \mathrm{mm}$
PB_P2	$0.4020\ \mathrm{mm}$	$-0.1868\ \mathrm{mm}$

Table 5.4: The relative difference from the standard position for the $R1$ PPA module.

Chapter 6

Outlook

This project includes the whole process of routine setting and demonstrated its reliability, yet a few tasks to be done show the necessity when this project is about to be put into use. Another method using a laser rangefinder is under evaluation and is expected to fulfil the requirements of the height metrology of the hybrids.

6.1 Remaining Challenges

The most important remaining task is to add the standard position of the hybrid fiducials to the post-process program, to produce a completely automatic system that can tell if certain module passes the metrology. It is about adding the positions of the items to be measured discussed in Chap.4.

During the process of the measurement, a difficulty arose as the XYZ coordinate form of the measurement is far from intuition, and it would take much effort to figure out if the operator came across a faulty result or where the fault is.

Based on the C++ program, it is possible to build up a graphical interaction user interface to illustrate the measurement, where OpenGL could be involved. A Python-C++ hybrid solution could be a more practical option.

Also, the standard model of the module could be added to this GUI as it can tell which item is beyond the threshold, which can provide a straightforward explanation of the situation of this sensor.

6.2 Comparison with Laser Rangefinder

A small group is working on the laser rangefinder method at Uppsala University for hybrid height metrology. An optoNCDT ILD1900-10 sensor by Micro-Epsilon is used to make a distance measurement, where the distance can be converted into the relative height.

The ILD1900-10 can measure the distance within the range of $20-30$ mm, with a linearity smaller than ± 2 μm and a repeatability better than 0.4 μm. This machine uses the principle of optical triangulation, that is, to project a point of light onto the surface and measure the position of this point with a separate image sensor. The position of the point of light seen from the image sensor is only decided by the distance between the surfaces to detect and this rangefinder.

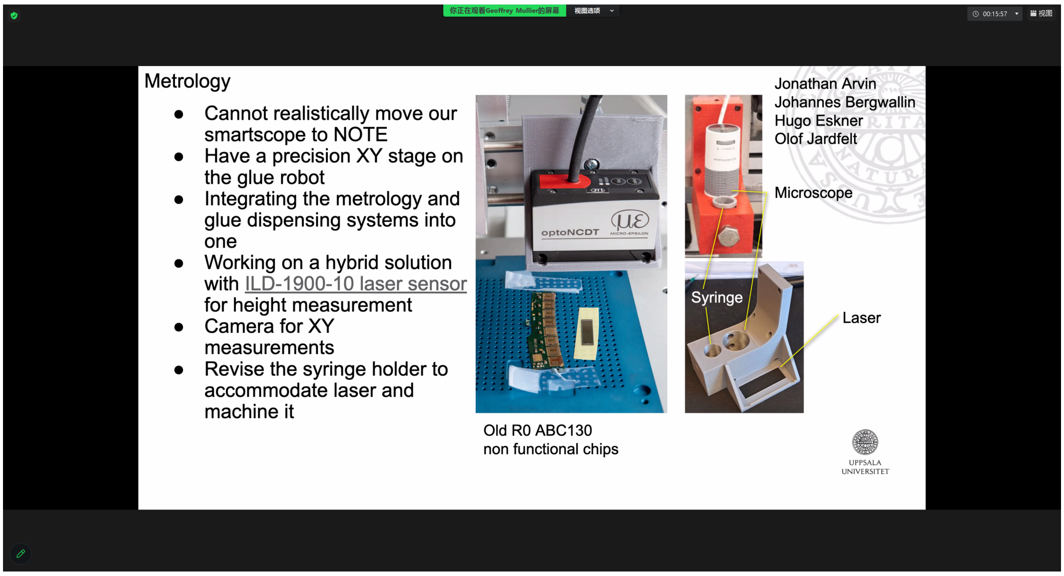

Figure 6.1: An early-stage test on the laser rangefinder done in Uppsala University. This is a slide page from the Scandinavian ITk week meeting.[24]

In principle, this rangefinder will return a distribution of the strength of this monochrome laser, which would have single or multiple peaks that indicate that one reflection happened. By a built-in algorithm or a proper analysis program, the distance(s) can be easily calculated.

This system will be used to scan through the hybrid, making a profile that includes all ASICs. The height difference between the ASIC top and PCB base will be calculated.

By now, the mechanism to mount the rangefinder has been tested, and a preliminary measurement done recently proved that the height difference can be detected, although not quite accurately with the rough experiment setting, as shown in the briefing (Fig.6.1-6.2) during the Nordic ITk week meeting.

After personnel in UU finish this method, a cross-check between this laser optical triangulation and the SmartScope auto-focusing can be achieved. By comparing these two methods,

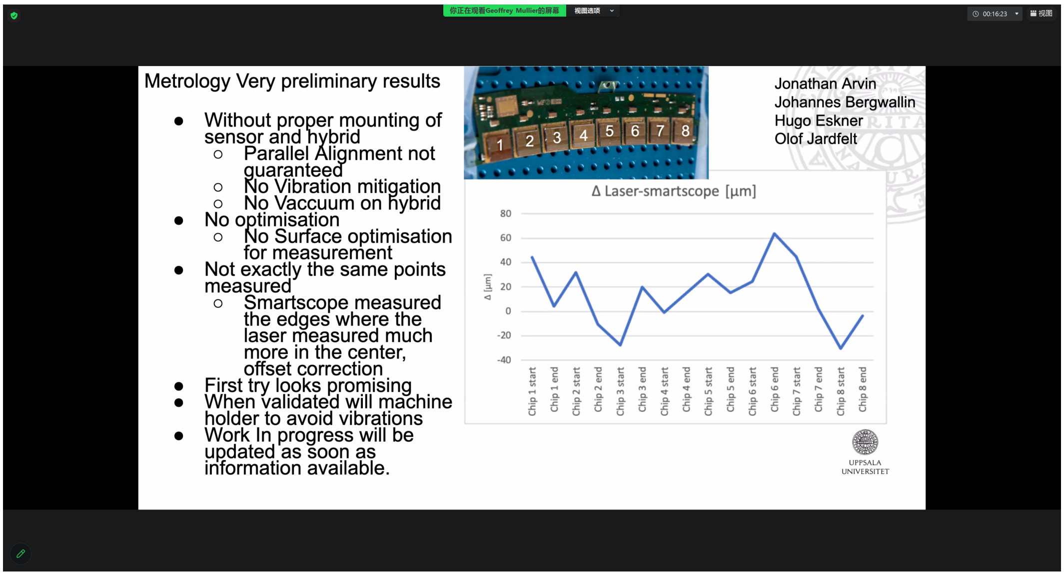

Figure 6.2: An early-stage test on the laser rangefinder done in Uppsala University. This is a slide page from the Scandinavian ITk weekly meeting.[24]

the laser method is more intended for hybrid height metrology, and the SmartScope is more for module planar metrology, yet the laser method can be easily implemented to the module height metrology. However, the laser rangefinder lack the ability to conduct XY plane measurement and will be attached to a camera or SmartScope to conduct the height measurement. This project demonstrated the power of the SmartScope on XY plane measurement and the SmartScope is very likely to be deployed for the metrology test in production, while the laser method is superior in Z-axis measurement by principle. A combination of the two methods can be expected afterwards as either has irreplaceable advantages in measurement.

Bibliography

[1] Chen-Ning Yang and Robert L Mills. "Conservation of isotopic spin and isotopic gauge invariance". In: Physical review 96.1 (1954), p. 191.

[2] Sheldon L Glashow. "Partial-symmetries of weak interactions". In: Nuclear physics 22.4 (1961), pp. 579–588.

[3] Steven Weinberg. "A model of leptons". In: Physical review letters 19.21 (1967), p. 1264.

[4] A Salam and N Svartholm. "Elementary Particle Physics: Relativistic Groups and Analyticity, Eight Nobel Symposium". In: Stockholm: Almquvist and Wiksell. p367 (1968).

[5] Shahriar Abachi et al. "Observation of the top quark". In: Physical review letters 74.14 (1995), p. 2632.

[6] Fumio Abe et al. "Observation of top quark production in p p collisions with the Collider Detector at Fermilab". In: Physical review letters 74.14 (1995), p. 2626.

[7] K Kodama et al. "Observation of tau neutrino interactions". In: Physics Letters B 504.3 (2001), pp. 218–224.

[8] M Benedikt et al. LHC Design Report. Tech. rep. CERN-2004-003. CERN, Geneva, 2004.

[9] The LHC conceptual design report. Tech. rep. CERN/AC/95-05(LHC). LHC Study Group et al., 1995.

[10] Technical design report for the ATLAS inner tracker strip detector. Tech. rep. ATL-TDR-025. LHC/ATLAS Experiment, 2017.

[11] Georges Aad et al. "Observation of a new particle in the search for the Standard Model Higgs boson with the ATLAS detector at the LHC". In: Physics Letters B 716.1 (2012), pp. 1–29.

[12] Serguei Chatrchyan et al. "Observation of a new boson at a mass of 125 GeV with the CMS experiment at the LHC". In: Physics Letters B 716.1 (2012), pp. 30–61.

[13] The High-Luminosity LHC Project. June 2016. URL: https://cds.cern.ch/record/2199189.

[14] Georges Aad et al. “The ATLAS experiment at the CERN large hadron collider”. In: Jinst 3 (2008), S08003.

[15] ITk Pixel Layout Updates. Tech. rep. ATLAS-P2-ITK-23-00-00. CERN, 2020.

[16] QC: Metrology Procedures - Modules. Tech. rep. AT2-IS-EP-0067 v.3.2. LHC/ATLAS Experiment, 2021.

[17] MeasureMind 3D MultiSensor Training Workbook. Seventh Printing. July 2005.

[18] MeasureMind 3D MultiSensor Reference Guide. Thirteenth Printing. Dec. 2006.

[19] PI 200 interface for the TP200 system. 2007. URL: https://www.renishaw.com/media/pdf/en/76a56f40b2724576968fcb34d37d2afc.pdf.

[20] SmartScope Vatnage 250. 2022. URL: https://www.ogpnet.com/products/metrology-systems/multisensor-metrology-systems/smartscope-video-multisensor-systems/smartscope-quest-vantage-systems/smartscope-vantage-250/.

[21] SmartScope Flash 200. 2023. URL: https://www.ogpnet.com/products/metrology-systems/multisensor-metrology-systems/smartscope-video-multisensor-systems/smartscope-flash/smartscope-flash-200/.

[22] Eigen Project. Eigen. URL: https://eigen.tuxfamily.org/index.php?title=Main_Page.

[23] Xiangyu Xu. XXY98/Atlasmodulemetrology-Lu. URL: https://github.com/xxy98/ATLASModuleMetrology-LU.

[24] ITk Weekly Meeting Briefing, 2023-05-02. Tech. rep. Uppsala University, 2023.

Acknowledgements

This project is supervised by Hannah Herde of Division of Particle Physics at Lund University. Hereby I'd like to address my appreciation for all of her guidance, help and support. This project will be impossible without her.

During this project, Lennart Österman of Division of Particle Physics at Lund University provided generous help in terms of engineering and technology. Much progress of this project comes from his effort and help.

The LHC is an international project, and the ATLAS ITk also involves a few Nordic institutes. Craig Wiglesworth from Niels Bohr Institute at University of Copenhagen provided help during my multiple visits to their lab in NBI. Geoffrey Mullier from the Department of Physics and Astronomy at Uppsala University provided a lot of help during my week-long visit to the north, also he brought quite a few ideas for this project.

Although this project is my sole responsibility, other graduate students in the Division of Particle Physics at Lund University, namely Sten Åstrand, Erik Wallin and Edurado Torres Reoyo, helped with this project and I must say a "thank you" to them.

Ten thousands kilometres away from home, my parents, GAO Shan and XU Yi-Gang provided infinite emotional and economical support to me here in Sweden. By the time of finishing this thesis, I'm also about to decide my next period, and they understand and support every single decision I make. Speech seems to weak for me to express my gratitude.

Last but not least, I have to appreciate my friends, no matter online or offline, no matter in Sweden, China or any other corner in this world, no matter since when I met them - ten years ago or two months ago.

Appendix

The source code for the post-processing code can be acquired from:
https://github.com/xxy98/ATLASModuleMetrology-LU/tree/master

Here's a sample of the standard output:

```
#---Header
#---Header
EC or Barrel:                SE
Module Type:                 M1
Module ref. Number:          20USEM10000014
Date:                        2023-05-11T00:18:36.479250+0200
Institute:                   Uppsala Universitet
Operator:                    Xiangyu XU
Instrument type:             OGP SmartScope Flash 200
Run Number:                  3
Measurement program version: v.23.05.02
#---Positions
#Location          X [mm]        Y [mm]
H_R1H0_P1          +007.9933     -058.4501
H_R1H0_P2          +108.6223     -061.1865
H_R1H1_P1          +003.4518     -020.5517
H_R1H1_P2          +111.5746     -023.0756
PB_P1              +070.5149     -044.8933
PB_P2              +106.7850     -033.5342
#---Glue heights:
# Location     Type      X [mm]       Y [mm]       Z [mm]
Sensor         1         +001.9997    -012.6942    -000.0175
Sensor         1         +012.0008    -012.7856    -000.0185
Sensor         1         +022.0290    -011.5737    -000.0325
Sensor         1         +032.0001    -011.6648    -000.0420
Sensor         1         +041.9992    -011.7567    -000.0439
Sensor         1         +052.0126    -010.6076    -000.0504
Sensor         1         +062.0008    -010.6988    -000.0596
Sensor         1         +071.9990    -010.7901    -000.0654
Sensor         1         +081.9992    -010.8815    -000.0661
Sensor         1         +091.9999    -010.9734    -000.0689
Sensor         1         +101.9995    -011.0647    -000.0714
Sensor         1         +112.0019    -011.1560    -000.0731
```

```
Sensor          1          +008.4058     -068.0447     -000.0369
Sensor          1          +018.4033     -068.1355     -000.0382
Sensor          1          +028.4009     -068.2269     -000.0433
Sensor          1          +038.4019     -068.3189     -000.0485
Sensor          1          +048.4001     -068.4102     -000.0556
Sensor          1          +058.4013     -068.5015     -000.0659
Sensor          1          +068.4015     -068.5928     -000.0712
Sensor          1          +078.4002     -068.6840     -000.0754
Sensor          1          +088.4000     -068.7753     -000.0718
Sensor          1          +098.4006     -068.8671     -000.0657
Sensor          1          +108.4000     -068.9583     -000.0752
H_R1H0_0        2          +006.8150     -044.7521     +000.2775
H_R1H0_0        2          +007.0873     -047.4899     +000.2680
H_R1H0_0        2          +006.7547     -049.4385     +000.2587
H_R1H0_0        2          +007.1557     -050.5465     +000.2505
H_R1H0_1        2          +072.1924     -047.5061     +000.2674
H_R1H0_1        2          +075.7704     -047.9647     +000.2563
H_R1H0_1        2          +076.1744     -047.9676     +000.2457
H_R1H0_1        2          +079.7589     -048.0977     +000.2437
H_R1H0_2        2          +100.4650     -049.3626     +000.2256
H_R1H0_2        2          +106.5538     -049.7112     +000.2185
H_R1H0_2        2          +106.5442     -050.8208     +000.1940
H_R1H0_2        2          +100.7676     -050.2324     +000.2118
HCCR1H0_4       2          +013.2762     -044.5418     +000.3346
HCCR1H0_4       2          +019.2690     -044.9065     +000.3619
HCCR1H0_4       2          +018.9411     -049.2725     +000.3311
HCCR1H0_4       2          +013.2080     -049.2571     +000.3274
ABC_R1H0_0      2          +108.9720     -058.8738     +000.1971
ABC_R1H0_0      2          +108.6399     -061.1860     +000.1967
ABC_R1H0_0      2          +100.0062     -060.6219     +000.2464
ABC_R1H0_0      2          +100.1332     -057.8670     +000.2363
ABC_R1H0_1      2          +098.7966     -057.9526     +000.2467
ABC_R1H0_1      2          +098.5078     -060.2777     +000.2603
ABC_R1H0_1      2          +089.9632     -057.1173     +000.2729
ABC_R1H0_1      2          +089.9230     -059.9442     +000.2740
ABC_R1H0_2      2          +088.6166     -057.2503     +000.2767
ABC_R1H0_2      2          +088.3818     -059.5760     +000.2718
ABC_R1H0_2      2          +079.7682     -059.3532     +000.2918
ABC_R1H0_2      2          +079.7779     -056.5725     +000.2892
ABC_R1H0_3      2          +078.4340     -056.7330     +000.2907
ABC_R1H0_3      2          +078.2302     -059.0616     +000.3021
ABC_R1H0_3      2          +069.6180     -059.0267     +000.3055
ABC_R1H0_3      2          +069.5602     -056.2428     +000.2897
ABC_R1H0_4      2          +068.2317     -056.4090     +000.3080
ABC_R1H0_4      2          +068.0708     -058.7520     +000.3180
ABC_R1H0_4      2          +059.4639     -058.8788     +000.3105
ABC_R1H0_4      2          +059.3538     -056.1168     +000.2938
ABC_R1H0_5      2          +058.0161     -056.3084     +000.2795
ABC_R1H0_5      2          +057.9123     -058.6375     +000.2994
```

```
ABC_R1H0_5     2          +049.3008     -058.9493     +000.3227
ABC_R1H0_5     2          +049.1341     -056.1651     +000.2969
ABC_R1H0_6     2          +047.8164     -056.3970     +000.3061
ABC_R1H0_6     2          +047.7539     -058.7456     +000.3269
ABC_R1H0_6     2          +039.1462     -059.2183     +000.3255
ABC_R1H0_6     2          +038.9228     -056.4420     +000.3102
ABC_R1H0_7     2          +037.5880     -056.6971     +000.3126
ABC_R1H0_7     2          +037.5666     -059.0347     +000.3172
ABC_R1H0_7     2          +028.9846     -059.6817     +000.3272
ABC_R1H0_7     2          +028.7058     -056.9028     +000.3200
ABC_R1H0_8     2          +027.3646     -057.1919     +000.3186
ABC_R1H0_8     2          +027.4054     -059.5106     +000.3236
ABC_R1H0_8     2          +018.8309     -060.3487     +000.3312
ABC_R1H0_8     2          +018.4914     -057.5757     +000.3279
ABC_R1H0_9     2          +016.8650     -057.8892     +000.3311
ABC_R1H0_9     2          +016.9436     -060.2283     +000.3352
ABC_R1H0_9     2          +008.3854     -061.2141     +000.3226
ABC_R1H0_9     2          +007.9856     -058.4294     +000.3019
H_R1H1_0       2          +005.4948     -035.6457     +000.1983
H_R1H1_0       2          +005.1919     -032.9171     +000.2072
H_R1H1_0       2          +004.8454     -032.4559     +000.2064
H_R1H1_0       2          +004.4986     -029.8148     +000.2179
H_R1H1_1       2          +073.2578     -029.2904     +000.2266
H_R1H1_1       2          +076.7732     -029.2453     +000.2304
H_R1H1_1       2          +077.1818     -029.2882     +000.2290
H_R1H1_1       2          +080.7661     -029.3964     +000.1906
H_R1H1_2       2          +103.6004     -030.0596     +000.1454
H_R1H1_2       2          +103.5914     -031.0252     +000.1552
H_R1H1_2       2          +107.7876     -031.6469     +000.1445
H_R1H1_2       2          +108.7699     -031.4830     +000.1437
HCCR1H1_5      2          +011.4030     -034.9689     +000.2601
HCCR1H1_5      2          +011.4462     -030.2483     +000.2865
HCCR1H1_5      2          +017.4619     -030.6353     +000.3096
HCCR1H1_5      2          +017.1457     -034.9809     +000.2825
ABC_R1H1_0     2          +003.4460     -020.5533     +000.2996
ABC_R1H1_0     2          +003.5441     -022.8946     +000.2983
ABC_R1H1_0     2          +012.3986     -022.3006     +000.3332
ABC_R1H1_0     2          +012.0061     -019.5275     +000.3474
ABC_R1H1_1     2          +013.4077     -019.6637     +000.3553
ABC_R1H1_1     2          +013.4485     -021.9934     +000.3427
ABC_R1H1_1     2          +022.3208     -021.5491     +000.3279
ABC_R1H1_1     2          +022.1175     -018.7645     +000.3552
ABC_R1H1_2     2          +023.3731     -018.9486     +000.3561
ABC_R1H1_2     2          +023.3747     -021.2859     +000.3352
ABC_R1H1_2     2          +032.2467     -021.0106     +000.3368
ABC_R1H1_2     2          +031.9523     -018.2341     +000.3482
ABC_R1H1_3     2          +033.3350     -018.4100     +000.3530
ABC_R1H1_3     2          +033.3012     -020.7424     +000.3378
ABC_R1H1_3     2          +041.9426     -017.8478     +000.3240
```

```
ABC_R1H1_3     2          +042.1804     -020.6317     +000.3129
ABC_R1H1_4     2          +043.2441     -020.3847     +000.3070
ABC_R1H1_4     2          +043.3270     -018.0473     +000.3309
ABC_R1H1_4     2          +051.9216     -017.6504     +000.3614
ABC_R1H1_4     2          +052.1284     -020.4385     +000.3287
ABC_R1H1_5     2          +053.1700     -020.2132     +000.3238
ABC_R1H1_5     2          +053.2978     -017.8843     +000.3538
ABC_R1H1_5     2          +062.0190     -017.6383     +000.3215
ABC_R1H1_5     2          +062.0538     -020.4220     +000.2919
ABC_R1H1_6     2          +063.1201     -020.2225     +000.2909
ABC_R1H1_6     2          +063.2725     -017.8794     +000.3237
ABC_R1H1_6     2          +072.1448     -017.8111     +000.3137
ABC_R1H1_6     2          +071.9895     -020.6032     +000.2809
ABC_R1H1_7     2          +073.0319     -020.3969     +000.2905
ABC_R1H1_7     2          +073.2520     -018.0850     +000.3192
ABC_R1H1_7     2          +081.8367     -018.1636     +000.3154
ABC_R1H1_7     2          +081.8901     -020.9365     +000.2926
ABC_R1H1_8     2          +082.9464     -020.7784     +000.2866
ABC_R1H1_8     2          +083.2007     -018.4574     +000.3100
ABC_R1H1_8     2          +092.0472     -018.6898     +000.3014
ABC_R1H1_8     2          +091.8060     -021.4720     +000.2782
ABC_R1H1_9     2          +092.8596     -021.3309     +000.2816
ABC_R1H1_9     2          +093.1559     -019.0088     +000.3000
ABC_R1H1_9     2          +101.7673     -019.4182     +000.2634
ABC_R1H1_9     2          +101.6967     -022.1917     +000.2455
ABC_R1H1_10    2          +102.7640     -022.0767     +000.2373
ABC_R1H1_10    2          +103.0944     -019.7395     +000.2518
ABC_R1H1_10    2          +111.6767     -020.2885     +000.2608
ABC_R1H1_10    2          +111.5690     -023.0767     +000.2516
PB_0           2          +107.9425     -038.6696     +000.4289
PB_1           2          +093.6609     -045.2588     +000.4785
PB_2           2          +075.4004     -046.1000     +000.4250
PB_3           2          +076.3908     -031.8283     +000.4568
PB_4           2          +057.5172     -035.8066     +000.2729
#---Other heights:
# Location      Type      X [mm]        Y [mm]        Z [mm]
```